Benchmarking K_{DP} in Rainfall: a Quantitative Assessment of Estimation Algorithms Using C-Band Weather Radar Observations

Miguel Aldana[1], Seppo Pulkkinen[1], Annakaisa von Lerber[1], Matthew R. Kumjian[2], and Dmitri Moisseev[1, 3]

[1]Space Research & Observation Technologies, Finnish Meteorological Institute, Helsinki, Finland
[2]Department of Meteorology & Atmospheric Science, The Pennsylvania State University, Pennsylvania, United States
[3]Institute for Atmospheric & Earth system Research, University of Helsinki, Helsinki, Finland

Correspondence: Miguel Aldana (miguel.aldana@fmi.fi)

Abstract. Accurate and precise K_{DP} estimates are essential for radar-based applications, especially in quantitative precipitation estimation and radar data quality control routines. The accuracy of these estimates largely depends on the post-processing of the radar's measured Φ_{DP}, which aims to reduce noise and backscattering effects while preserving fine-scale precipitation features. In this study, we evaluate the performance of several publicly available K_{DP} estimation methods implemented in open-source libraries such as Py-ART and Wradlib, and the method used in the Vaisala weather radars. To benchmark these methods, we employ a polarimetric self-consistency approach that relates K_{DP} to reflectivity and differential reflectivity in rain, providing a reference self-consistency K_{DP} (K_{DP}^{sc}) for comparison. This approach allows for the construction of the reference K_{DP} observations that can be used to assess the accuracy and robustness of the studied K_{DP} estimation methods. We assess each method by quantifying uncertainties using C-band weather radar observations where the reflectivity values ranged between 20 and 50 dBZ.

Using the proposed evaluation framework we could define optimized parameter settings for the methods that have user-configurable parameters. Most of such methods showed significant reduction in the estimation errors after the optimization with respect to the default settings. We have found significant differences in the performances of the studied methods, where the best performing methods showed smaller normalized biases in the high reflectivity values (i.e., ≥ 40 dBZ) and overall smaller normalized root mean squared errors across the range of reflectivity values.

1 Introduction

The specific differential phase (K_{DP}) plays an important role in many weather radar applications, particularly in hydrometeor classification (Höller et al., 1994; Vivekanandan et al., 1999; Liu and Chandrasekar, 2000; Zrnić et al., 2001; Keenan, 2003; Lim et al., 2005; Tessendorf et al., 2005; Marzano et al., 2007; Dolan and Rutledge, 2009; Park et al., 2009; Snyder et al., 2010; Al-Sakka et al., 2013; Dolan et al., 2013; Thompson et al., 2014; Bechini and Chandrasekar, 2015; Grazioli et al., 2015; Wen et al., 2015; Besic et al., 2016; Ribaud et al., 2019) and quantitative precipitation estimation (QPE) (Sachidananda and Zrnić, 1987; Chandrasekar et al., 1990; Ryzhkov and Zrnić, 1995, 1996; May et al., 1999; Bringi and Chandrasekar, 2001; Bringi et al., 2006; Matrosov et al., 2006; Giangrande and Ryzhkov, 2008; Bringi et al., 2011; Cifelli et al., 2011; Wang et al., 2013;

Figueras I Ventura and Tabary, 2013; Chen and Chandrasekar, 2015; Chen et al., 2017; Thompson et al., 2018; Zhang et al., 2020), and is used in data assimilation for numerical weather prediction models (Thomas et al., 2020; Du et al., 2021) and in hydrological applications (Brandes et al., 2002; Ryzhkov et al., 2005b; Vulpiani et al., 2012; Li et al., 2023; Cremonini et al., 2023). Compared to radar power variables, i.e., reflectivity factor at horizontal polarization (Z_H) and differential reflectivity (Z_{dr}), K_{DP} offers advantages in terms of accuracy, resilience, and reliability due to its immunity to radar miscalibration, attenuation (Bringi and Chandrasekar, 2001; Illingworth, 2004; Ryzhkov and Zrnic, 2019), and partial beam blockage (Zrnić and Ryzhkov, 1996). It has also proven successful in hydrometeor classification routines (Lim et al., 2005; Park et al., 2009; Grazioli et al., 2015; Tiira and Moisseev, 2020), especially in the detection of graupel (Dolan and Rutledge, 2009; Oue et al., 2015), small melting hail (Kumjian et al., 2019), and dendritic growth zone and processes within (Kennedy and Rutledge, 2011; Andrić et al., 2013; Schneebeli et al., 2013; Moisseev et al., 2015; Kumjian and Lombardo, 2017). The ability of K_{DP} to accurately estimate heavy rainfall, differentiate hydrometeor types, and overcome attenuation in precipitation makes it an invaluable operational and research radar variable.

Despite its advantages, accurate estimation of K_{DP} from radar-measured differential phase (Φ_{DP}) remains challenging. Mathematically, K_{DP} is half the range derivative of Φ_{DP}, which measures the phase shift between horizontally and vertically polarized signals as they propagate through precipitation. This phase shift (Φ_{DP}) is influenced by hydrometeor concentration, shape, orientation, and composition (Kumjian, 2018). However, Φ_{DP} is not typically smooth and monotonically increasing along the rain path; it contains fluctuations due to noise (ϵ) and backscattering differential phase (δ_{HV}) (Ryzhkov and Zrnić, 1996; Ryzhkov and Zrnic, 1998). Excessive filtering of Φ_{DP} to remove ϵ can lead to the loss of fine-scale precipitation features, affecting the accuracy of K_{DP} estimates especially in light precipitation (Huang et al., 2017). In heavier precipitation, δ_{HV} causes spikes in Φ_{DP}, especially at higher radar frequencies, further complicating accurate K_{DP} estimation (Bringi and Chandrasekar, 2001).

To address these challenges, various methods have been developed to post-process Φ_{DP} and derive K_{DP} (Hubbert et al., 1993; Hubbert and Bringi, 1995; Ryzhkov et al., 2005c; Wang and Chandrasekar, 2009; Otto and Russchenberg, 2011; Maesaka et al., 2012; Vulpiani et al., 2012; Schneebeli and Berne, 2012; Giangrande et al., 2013; Schneebeli et al., 2014; Huang et al., 2017; Reinoso-Rondinel et al., 2018; Wen et al., 2019). Basic approaches include median filters and moving windows, while more advanced methods use regression techniques and self-consistency constraints based on Z_H or Z_{dr}. Many of these methods are now available in open-source Python libraries such as Py-ART (Helmus and Collis, 2016) and Wradlib (Heistermann et al., 2013). For this study, some of the most popular implemented methods based on Maesaka et al. (2012), Vulpiani et al. (2012), Giangrande et al. (2013), and Schneebeli et al. (2014) were selected for analysis. Additionally, the K_{DP} product implemented by Vaisala in IRIS software (Vaisala, 2017) based on Wang and Chandrasekar (2009) was also included in our analysis. Each algorithm has its own data requirements, mathematical approach, and optimizing parameters, raising the question of which performs optimally under varying parameter settings, and rainfall intensities.

Recent studies show that K_{DP} estimates can vary significantly depending on the algorithm and the optimizing parameters used. Reimel and Kumjian (2021) evaluated the errors of several methods using synthetic K_{DP} profiles and found that no single algorithm was optimal across all rainfall conditions. Instead, performance varied with the complexity of the rain profile and selected parameters. They identified kdp_maesaka (Py-ART's implementation of Maesaka et al. (2012)) and phase_proc_lp (Py-ART's implementation of Giangrande et al. (2013)) as particularly versatile. However, Reimel and Kumjian (2021) used synthetic data, which may miss some of the effects present in radar observations of rainfall (e.g., δ_{HV}). More recently, Li et al. (2023) compared kdp_maesaka and phase_proc_lp in an extreme summer rainfall event, finding that fine-tuning the methods played a key role in retrieving the most accurate K_{DP} estimate. Despite these insights, the performance and uncertainties of most methods in rainfall observations remain largely unexplored.

The goal of this study is to evaluate the performance of publicly available K_{DP} estimation methods in real rainfall observations and quantify their uncertainties as a function of reflectivity intensities. To achieve this, we employ a benchmarking K_{DP}, herein K_{DP}^{sc}, computed from measured Z_H and Z_{dr} and using self-consistency relations in rain. In rainfall observations, the polarimetric radar variables are not independent, but one can be computed in terms of the others via the so-called self-consistency relations (Aydin et al., 1987; Scarchilli et al., 1993). These relations have proven successful in hydrometeor classification (Aydin and Giridhar, 1992) and radar calibration correction (Gorgucci et al., 1992) routines. For instance, Aydin and Giridhar (1992) showed that the hydrometeors can be classified based on their proximity to clusters around self-consistency curves between polarimetric variables. At nearly the same time, Gorgucci et al. (1992) noted the self-consistency of Z_H, Z_{dr} and K_{DP} in rainfall and proposed a method to calibrate Z_H and correct Z_H-rainfall estimates benchmarking against K_{DP}-rainfall estimates. Thereafter, several methods linking the polarimetric variables via self-consistency relations have been widely used to calibrate Z_H (Goddard et al., 1994; Scarchilli et al., 1996; Vivekanandan et al., 2003; Ryzhkov et al., 2005a; Gourley et al., 2009). In this study, K_{DP}^{sc} is computed using the consistency relation linking K_{DP} to Z_H and Z_{dr}, firstly noted by Goddard et al. (1994) and described in Gourley et al. (2009), requiring thorough selection and filtering of Z_H and Z_{dr}. K_{DP}^{sc} computed from quality-controlled Z_H and Z_{dr} measurements provides a solid benchmark against which to compare the methods' performances, select optimal parameters, and quantify the associated uncertainties.

This paper is organized as follows: Section 2 describes the radar and disdrometer data, the evaluation framework, and introduces the K_{DP} estimation methods. Section 3 presents and discusses the parameter optimization and performance evaluation of the methods, and Section 4 summarizes the findings.

2 Data & Methods

2.1 Radar & Disdrometer Data

This study evaluates the performance of K_{DP} estimation methods using real rainfall data. The dataset was collected from the Finnish Meteorological Institute's (FMI) C-band Vantaa radar, located near Helsinki, Finland (see Fig. 1). The radar recorded
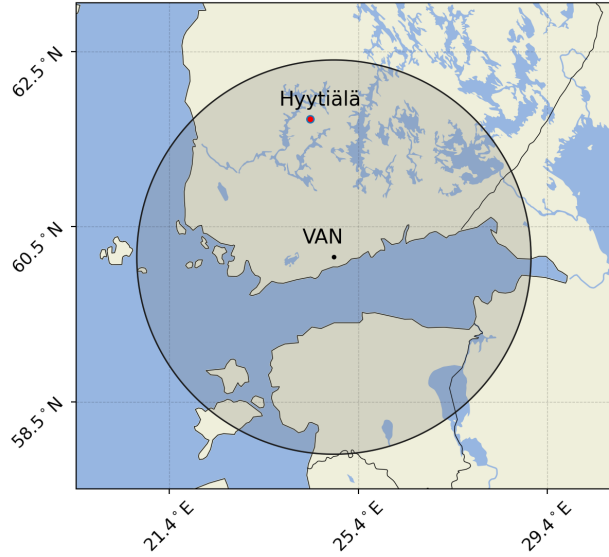
Figure 1. Map showing locations of FMI's Vantaa radar (VAN) and Hyytiälä's research station where DSD data were collected. The shaded area is a circle of 250 km radius corresponding to the spatial coverage of the radar.

various quantities, including Z_H, Z_{dr}, Φ_{DP}, K_{DP}, cross-correlation coefficient (ρ_{HV}), and the hydrometeor classification product available in IRIS (Vaisala, 2017) and based on the methodology described by Chandrasekar et al. (2013). The spatial resolution of the radar is 500 meters in range and $1°$ in azimuth, with scans performed every 5 minutes, and the data was
95   collected with an elevation angle of $0.7°$. The dataset spans from June to September during the years 2017 to 2019, capturing precipitation events with variable rainfall intensities and spatial extents. The raw radar dataset as well as the post-processed K_{DP} estimates are available from the link provided in Aldana (2024).

To ensure data quality, only periods when the Vantaa radar had calibration errors within 1 dB were selected. The calibra-
100   tion was verified by i) identifying periods where solar flux estimates from Vantaa radar estimates aligned consistently with Dominion Radio Astrophysical Observatory (DRAO) estimates (Huuskonen and Holleman, 2007; Tapping, 2013; Holleman et al., 2022), and ii) selecting radar scans within these periods where Z_H-calibration offsets were within 1 dB, following the absolute calibration procedure outlined by (Gourley et al., 2009). Z_{dr} bias was estimated and corrected during these periods by computing the offset between observed and self-consistency Z_{dr}, derived from observed Z_H, as described in (Hickman, 2015)
105   and computing the average for several cases.

The performance of the K_{DP} estimation methods is benchmarked against self-consistency K_{DP}^{sc}, computed from measured Z_H, Z_{dr} and using self-consistency relations in rain. The self-consistency relations, which link the polarimetric radar variables, were derived by fitting radar variables computed using the open-source library, PyTMatrix (Leinonen, 2014). PyTMatrix

110   provides a simple interface for T-Matrix electromagnetic scattering calculations (Waterman, 1965; I. Mishchenko et al., 2000), requiring the user to provide drop size distribution (DSD) data and setting parameters such as temperature, radar wavelength's band and raindrop shape model. The parameters used for the T-Matrix calculations were $10°C$, C-band and Thurai et al. (2007), respectively, and the DSD data provided was collected by an optical Parsivel disdrometer (Moisseev, 2024) located in Hyytiälä, Finland (see Fig. 1).

115

The Parsivel disdrometer records the number of particles and velocity at one-minute intervals, sorting the data into 32 bins depending on particle's size (i.e., equivalent volume diameter) and 32 additional bins depending on particle's fall velocity. From the number of particles, size and velocity classes, the Parsivel disdrometer computes the precipitation type, which was used to filter out non-liquid particles. Observations were further limited to times when the 30-minute average 2-meter temper-

120   ature exceeded $2°C$ to ensure liquid rain. Following the filtering procedure to reduce statistical errors suggested by Leinonen et al. (2012), only those measurements with at least 100 counts in two consecutive bins and positive counts in at least four consecutive bins were retained. The disdrometer dataset, covering June to September from 2014 to 2019, provided a robust basis for deriving average summer-season DSD parameters such as mean volume diameter (D_0), intercept parameter (N_w), and shape parameter (μ). These parameters showed strong agreement with those reported by Leinonen et al. (2012) in a clima-

125   tological study of Finland. From the derived DSD parameters (N_w, D_0, and μ), the polarimetric radar variables were computed and used for deriving the self-consistency relation defining the framework to evaluate the K_{DP} estimation methods.

2.2 K_{DP} Evaluation Framework

The performance of K_{DP} estimation methods is evaluated using K_{DP}^{sc} as benchmark. This quantity is calculated from each radar-measured tuple (Z_H, Z_{dr}) following a relationship of the form (Goddard et al., 1994; Illingworth and Blackman, 2002;

130   Gourley et al., 2009):

$$K_{DP}^{sc} = z_H \times 10^{-5} \times (a_1 + a_2 \times Z_{dr} + a_3 \times Z_{dr}^2 + a_4 \times Z_{dr}^3), \tag{1}$$

where $z_H = 10^{0.1 \times Z_H}$ represents Z_H in linear units ($mm^6 m^{-3}$) and Z_{dr} is in decibels (dB). The coefficients used in this relation are $a_1 = 6.78$, $a_2 = -2.65$, $a_3 = 0.562$ and $a_4 = -0.0624$. The coefficients align well with those reported by Gourley et al. (2009), which employed the raindrop shape models by Brandes et al. (2002) and Thurai and Bringi (2005).

135

To ensure the accuracy and robustness of K_{DP}^{sc} estimates used in the method assessment, it was crucial to quality-control the Z_H and Z_{dr} data. Radar observations of rain are often affected by non-meteorological measurements, resonance effects, and hail contamination (Bringi and Chandrasekar, 2001; Kumjian, 2013; Ryzhkov and Zrnic, 2019). To address these issues, the following filtering steps were applied:

140   – *Noise filtering*: A minimum threshold of 0.97 was applied to ρ_{HV}.

– *Non-meteorological observations filtering*: The hydrometeor classification product from IRIS (Vaisala, 2017), based on Chandrasekar et al. (2013), was used to exclude gates classified as non-meteorological.

- *δ_{HV} reduction*: Gates with $Z_{dr} > 3.5$ dB were excluded (Bringi and Chandrasekar, 2001; Gourley et al., 2009).

- *Non-liquid rain filtering*:

  - Only radar scans from the warm months (Jun-Sep) were selected.

  - Gates not classified as rain by the hydrometeor classification product were excluded.

  - Hail contamination was addressed by removing gates with $Z_H \geq 50$ dBZ.

  - Observations from the melting layer and above were suppressed by masking gates farther than 70 km (see last dashed ring in Fig. 2) from the radar in the radial direction. The distance was manually set by identifying gates with melting layer signatures (Giangrande et al., 2008; Boodoo et al., 2010).

In addition to addressing noise and non-liquid rain measurements, K_{DP}^{sc} estimates are affected by attenuation in Z_H and differential attenuation in Z_{dr}, particularly in cases of heavy rainfall, extended propagation paths through rain (hereafter "rain paths") (Zrnić and Ryzhkov, 1996; Carey et al., 2000; Bringi and Chandrasekar, 2001; Kumjian, 2013), and when the radar's antenna radome is wet (Blevis, 1965; Kurri and Huuskonen, 2008). To mitigate these effects, radar scans when there was rain on top of the radar within the past 20 minutes were discarded. Then, for the remaining cases, attenuation in heavy precipitation or extended rain paths were addressed by flagging the radar gates when suspected attenuation of at least 1 dB was detected. The attenuation in range gates was inferred using a standard method that linearly relates the losses in Z_H and Z_{dr} with increases in $\Delta\Phi_{DP}$ (Ryzhkov and Zrnić, 1995; Carey et al., 2000; Bringi and Chandrasekar, 2001; Gourley et al., 2009). $\Delta\Phi_{DP}$ corresponds to the total span of Φ_{DP} along the radial within a rain path. A rain path was defined as a set of consecutive gates with rain features extending at least 20 km in the radial direction. For C-band radar, a minimum threshold of $12°$ in $\Delta\Phi_{DP}$ indicates attenuation of at least 1 dB (Carey et al., 2000). In this study, a threshold of $10°$ was used, meaning that gates within rain paths featuring $\Delta\Phi_{DP} \geq 10°$ were flagged as attenuated.

An example of the filtering procedure applied to a radar scan is shown in Fig. 2. This figure demonstrates the effects of the filtering process and considered attenuation on the chosen data samples.

Following the filtering process, the dataset comprised 652,624 quality-controlled gates from 70 radar scans. Figure 3 presents a histogram of the data proportions across different Z_H values, showing the highest percentage of data between 30-35 dBZ, with a sharp decrease from 35-50 dBZ. The stacked bars indicate the percentages of attenuated and non-attenuated gates, with the ratio of attenuated to non-attenuated data increasing with greater Z_H.

2.3 K_{DP} Estimation methods

This Section provides an overview of the K_{DP} estimation methods selected for this study. The selection criteria focused on the availability of these methods in widely used open-source libraries, such as Py-ART (Helmus and Collis, 2016) and Wradlib
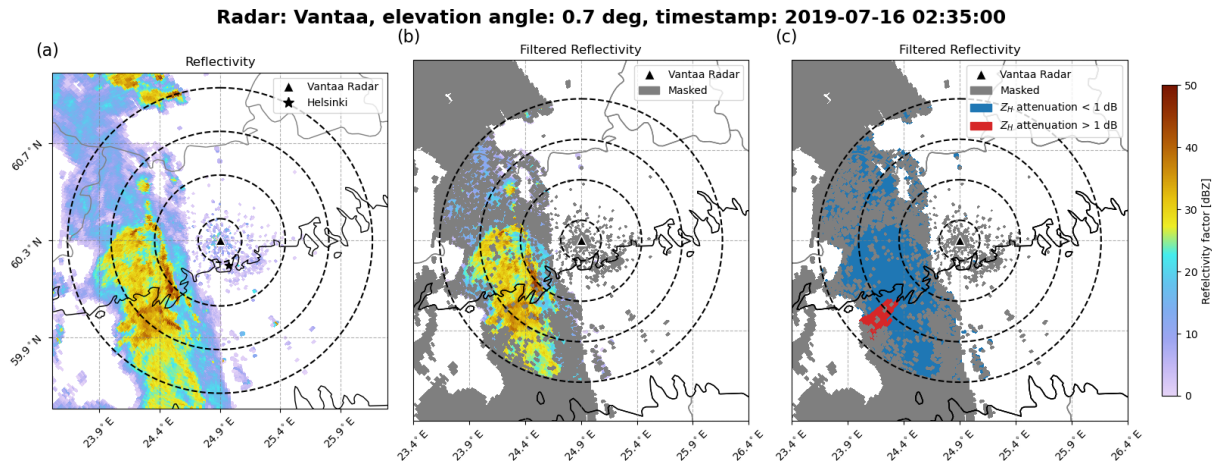
Figure 2. Example of a Vantaa radar scan during a precipitation event on the 16 July 2019 at an elevation angle of $0.7°$. Panel (a) shows measured Z_H; panel (b) shows filtered Z_H with masked gates in grey; panel (c) shows the same as (b) but with attenuated gates marked in red and non-attenuated gates marked in blue. Dashed rings represent radial distances of 10, 30, 50 and 70 km from the radar.
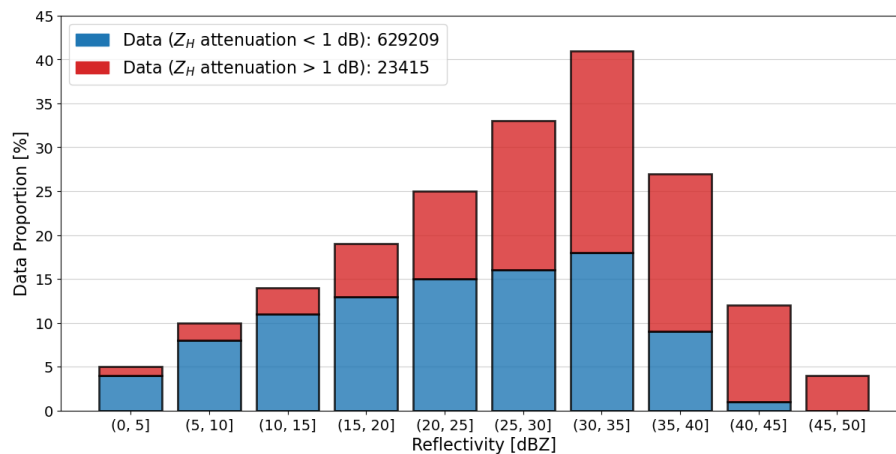
Figure 3. Proportion of data across Z_H intervals of 5 dBZ. Attenuated data is represented by red bars and non-attenuated data is represented by blue bars. The legend indicates the total number of gates with suspected attenuation of at least 1 dB (red) and less than 1 dB (blue).

175   (Heistermann et al., 2013). At the time of this study, Py-ART version 1.17.0 included the following methods: kdp_maesaka, kdp_vulpiani, phase_proc_lp and kdp_schneebeli. Wradlib version 2.0.3 included kdp_from_phidp and phidp_kdp_vulpiani. However, phidp_kdp_vulpiani was excluded from our analysis, as it is based on the same method proposed by Vulpiani et al. (2012) that is already represented by Py-ART in kdp_vulpiani. Additionally, kdp_iris, a method based on Wang and Chandrasekar (2009) and implemented by Vaisala in the IRIS software (Vaisala, 2017) was included. Table 1 summarizes the key

180   features of the selected methods and a brief description of the methods is provided below.

Table 1. List of K_{DP} methods studied with key features.

Method	Source	Data pre-requisites	Precipitation Type	Mathematical Approach (constraints)	Tested Parameters
kdp_maesaka	Py-ART	Unfolded ϕ_{DP}	liquid	Variational	*clpf*
kdp_vulpiani	Py-ART	Pre-filtered Ψ_{DP}	Any	Moving window	*windsize*, *n_iter*
phase_proc_lp	Py-ART	Unattenuated Z_H	liquid	Linear Programming ($K_{DP}(Z_H)$)	*self_const*, *coef*, *window_len*
kdp_from_phidp	Wradlib	No NaN values	Any	Moving window	*winlen*, *dr*
kdp_schneebeli	Py-ART	Pre-filtered Ψ_{DP}	Any	Kalman filter	-
kdp_iris	IRIS	-	Any	Adaptive regression	-

a. **kdp_maesaka**. Developed by Maesaka et al. (2012) and available in Py-ART, this method estimates non-negative K_{DP} from liquid precipitation measurements. It addresses the issue of negative K_{DP} estimates observed in exclusively liquid precipitation regions when using classical methods based on iterative filtering and local linear regression. Maesaka et al. (2012) identified that negative K_{DP} were caused by noise in Φ_{DP} during weak precipitation and δ_{HV} during heavy precipitation. The method restricts K_{DP} to positive values and assumes that Φ_{DP} is a monotonically increasing function with range, already unfolded.

b. **kdp_vulpiani**. Developed by Vulpiani et al. (2012) and available in Py-ART, this method estimates K_{DP} for any type of precipitation. It uses a multistep, moving-window range derivative approach to obtain K_{DP}. It calculates a K_{DP} profile from the range derivative of a noise-reduced, offset-corrected, and unfolded Φ_{DP} profile. At each window, K_{DP} is compared to thresholds representing unrealistic K_{DP} values within precipitation, correcting possible aliasing with the minimum threshold.

c. **phase_proc_lp**. Developed by Giangrande et al. (2013) and available in Py-ART, this method estimates non-negative K_{DP} from liquid precipitation measurements. It uses a linear-programming (LP) method to enforce monotonic behavior in Φ_{DP}, restricting K_{DP} to positive values. It extracts δ_{HV} from Φ_{DP} and it uses self-consistency constraints to bound K_{DP} estimates based on measured Z_H. The method requires quality-controlled Z_H and allows user-defined thresholds to exclude hail and set the environmental $0\,°C$ level to exclude mixed-phase particles.

d. **kdp_from_phidp**. Implemented in wradlib (Heistermann et al., 2013) based on Vulpiani et al. (2012), this method estimates K_{DP} for any type of precipitation. It computes range-wise differentiation of Φ_{DP} over a user-defined window size length, defaulting to 7 gates for a range resolution of 1 km. Unlike kdp_vulpiani, it allows the selection of the method for range-gate differentiation, albeit it does not support multiple iterations, prioritizing speed over phase unfolding and noise issues in Φ_{DP}.

e. **kdp_schneebeli**. Developed by Schneebeli et al. (2014) and available in Py-ART, this method estimates K_{DP} for any type of precipitation. It selects the best-averaged K_{DP} profile from forward and backward propagation Kalman-filtered estimates. The Kalman filters are applied twice to each range gate state (accounting for forward and backward propagation) multiple times, recalculating the covariance matrices each time to yield unique states, and the best estimate is selected.

f. **kdp_iris**. Implemented in the Vaisala's software IRIS (Vaisala, 2017) and based on Wang and Chandrasekar (2009), this method estimates K_{DP} for any type of precipitation. It computes K_{DP} adaptively through piece-wise regression and a regularization framework that minimizes both smoothness in Φ_{DP} and regression errors. The regularization adapts based on range variations in K_{DP} and ρ_{HV} measurements, preserving steep Φ_{DP} changes in high-intensity precipitation while reducing variations in low-intensity precipitation.

3 Results

3.1 Parameter Optimization of methods

All the methods except kdp_iris are available in open source libraries and feature user-configurable parameters to improve the K_{DP} estimates. However, two methods are excluded from the optimization: kdp_schneebeli and kdp_iris. In kdp_schneebeli, the error covariance matrix of the measurements ($rcov$) and state transitions ($pcov$) require a large ensemble of stochastic simulated rainfall fields to derive them. Since such information is not available to us, we use the method with default settings. In kdp_iris, the end-user has no effect on the derivation of K_{DP}. Instead, at the FMI we use the K_{DP} product as it comes from the IRIS software (Vaisala, 2017). Therefore, the optimization focuses on the methods kdp_maesaka, kdp_vulpiani, phase_proc_lp and kdp_from_phidp and in this Section, we quantify the errors under varying parameter settings, and select the optimal values.

First, a qualitative analysis is provided with the use of K_{DP} vs. Z_H scatter plots, illustrating the relationship between estimated K_{DP} (y-axis) and Z_H (x-axis), and benchmarking against K_{DP}^{sc} (dashed black line). Then, the errors of each method as a function of parameter setting and Z_H is provided. To achieve this, the dataset was divided into six 5-dB intervals ranging from 20 to 50 dBZ; we then computed for each interval the root mean square error (RMSE) and mean error (herein bias) and normalized by the mean K_{DP}^{sc} from each interval. The optimal parameters were selected based on the smallest averaged normalized RMSE (herein NRMSE) in the last three Z_H intervals (i.e., 35-50 dBZ), prioritizing the accuracy of K_{DP} estimates in high-intensity precipitation.

The tested settings for kdp_maesaka, kdp_vulpiani, phase_proc_lp and kdp_from_phidp are summarized in Table 2, indicating the tested values, the default value(s) used in the implementation and the optimal value(s) found in this study.

Table 2. Summary of the parameter's settings for each of the optimized methods.

Method	Parameter(s) Tested	Tested Values	Default	Optimal
kdp_maesaka	$clpf$	$\{10^{-2}, 10^{-1}, 10^0, 10^1, 10^2, 10^3, 10^4, 10^5\}$	10^0	10^{-2}
kdp_vulpiani	$windsize$	$\{2, 6, 10, 14\}$	10	10
	n_iter	$\{2, 6, 10, 14\}$	10	2
phase_proc_lp	$window\_len$	$\{5, 10, 15, 20, 25, 30, 35, 40\}$	35	5
kdp_from_phidp	$winlen$	$\{3, 7, 11\}$	7	11
	dr	$\{0.5, 1, 2, 4\}$	1.0	2

3.1.1 Py-ART's Maesaka method

Py-ART's implementation of Maesaka et al. (2012), kdp_maesaka, features the optimizing parameter $Clpf$, which regulates the low-pass filter in Φ_{DP}. The low-pass filter controls the degree of smoothing of Φ_{DP}, with higher $Clpf$ values producing smoother Φ_{DP} profiles. In kdp_maesaka, the default value of $Clpf$ is 1.0, and this value is scaled by the range resolution of

235   the radar to match the resolution of the constraints applied to Φ_{DP}. The scaling is proportional to the fourth power of the range resolution of the radar, and if we were to compare to the values used in Maesaka et al. (2012), a value of 1.0 corresponds to 10^{10} for Vantaa radar's range resolution of 500 m. In Maesaka et al. (2012), $Clpf$ values from 10^9 to 10^{13} were tested on one rainfall case using a 250-m range resolution X-band radar. Their results show that values closer to 10^{13} suppressed fine-scale precipitation features while producing a smooth and clean K_{DP}, whereas values closer to 10^9 preserved fine-scale features

240   while substantially including more noise. These results lead us to test values from 10^8 to 10^{15}, corresponding to 10^{-2} and 10^5 in kdp_maesaka accounting for Vantaa's radar range resolution. Figure 4(a)-(h) shows scatter plots of K_{DP} estimates using kdp_maesaka as a function of Z_H for different $Clpf$ values. All scatter plots show overall accurate and precise K_{DP} estimates within the Z_H range 0-30 dBZ. This result implies that the subset of $Clpf$ values studied produce sufficiently smoothed Φ_{DP} to reduce the impact of noise in light precipitation. However, the effects of excessive smoothing are observed at the range of

245   40-50 dBZ, where K_{DP} noticeably underestimates K_{DP}^{sc}. By comparing the scatter plots from $Clpf = 10^{-2}$ to $Clpf = 10^5$ in the Z_H interval 40-50 dBZ, the underestimation of K_{DP} is stronger with increasing $Clpf$.

To capture the influence of $Clpf$ on the errors when estimating K_{DP} as a function of precipitation intensity, Figs. 5(a) and 5(b) show NRMSE and normalized bias of K_{DP} estimates with varying $Clpf$. The smaller and consistent NRMSEs in regions

250   of $Z_H \geq 35$ dBZ in Fig. 5(a) indicate that kdp_maesaka reaches stable solutions for all $Clpf$ values tested. However, $Clpf$ of 10^5 showed the largest variability when transitioning from lowest to highest Z_H among the values tested, producing largest NRMSE for $Z_H \geq 35$ dBZ and lowest otherwise. The underestimation of K_{DP} using 10^5 is evidenced in Fig. 5(b) for $Z_H \geq 35$ dBZ, where the results were the most negatively biased. The biases from the remaining parameters were equally consistent and smaller.
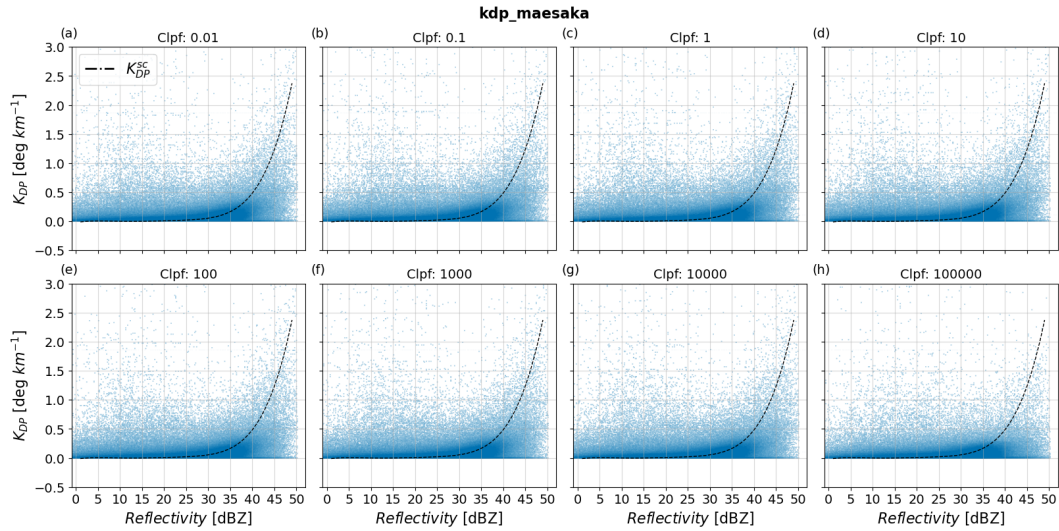
Figure 4. Scatter plots of estimated K_{DP} from kdp_maesaka as function of reflectivity and for various values of $Clpf$. The panels (a)-(h) show results with C_{lfp} values from 10^{-2} to 10^5. The dashed black line corresponds to K_{DP}^{sc}.
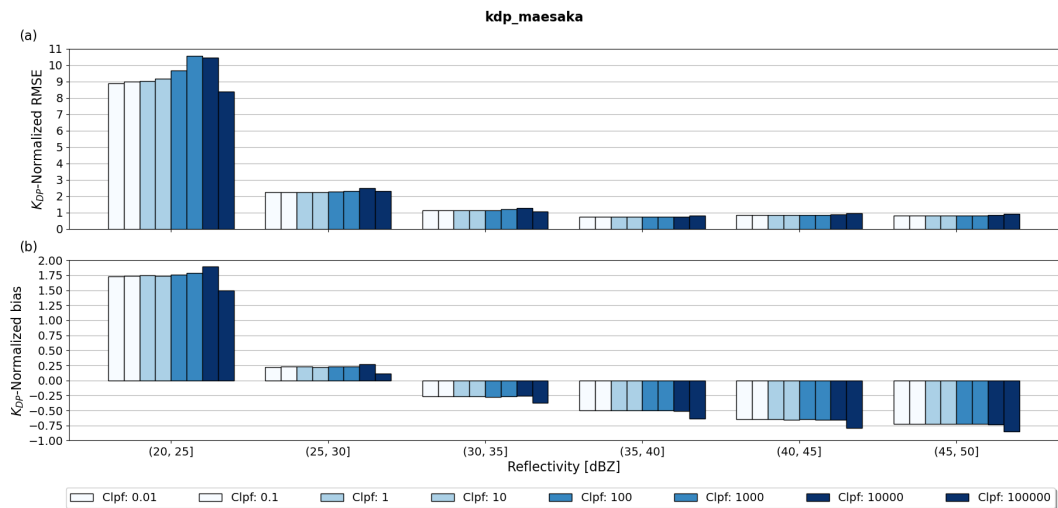
Figure 5. Panel (a) shows RMSE normalized by interval-averaged K_{DP}^{sc} of kdp_maesaka relative to K_{DP}^{sc} as a function of reflectivity and for various values of $Clpf$; panel (b) shows same as (a) but for the normalized bias metric.

255

Our results show that larger values of $Clpf$ lead to larger errors due to oversmoothing in Φ_{DP}. Overall, kdp_maesaka performs consistently when precipitation intensities reach 35 dBZ. The $Clpf$ yielding the smallest 35-50-dBZ-averaged NRMSE was 10^{-2}.

3.1.2 Py-ART's Vulpiani method

260 Py-ART's implementation of Vulpiani et al. (2012), kdp_vulpiani, features two optimizing parameters: *windsize* (number of gates used for estimating K_{DP}) and *n_iter* (number of re-estimations of K_{DP} per window). Higher values of these parameters result in smoother Φ_{DP} profiles. Reimel and Kumjian (2021) found various parameter combinations worked well depending on precipitation complexity, leading us to test combinations from 2 to 14 for both parameters. Figure 6(a)-(p) shows scatter plots comparing the performance of kdp_vulpiani for different values of *windsize* and *n_iter* in estimating K_{DP}. Figure

265 6(a) shows the scatter of K_{DP} using the largest tested settings, whereas Fig. 6(p) shows the results for the smallest. Each row holds *windsize* constant while each column holds *n_iter* constant. In the scatter plot from Fig. 6(a) with *windsize* = 14 and *n_iter* = 14, the data is predominantly clustered under K_{DP}^{sc} for $Z_H \geq 35$ dBZ, indicating underestimation of K_{DP}. For $Z_H <35$ dBZ, this parameter setting produces accurate and precise results. The scatter plots for smaller setting values, i.e., towards Fig. 6(p), are slightly more accurate albeit significantly less precise; the scatter plot from Fig. 6(p) with *windsize* = 2

270 and *n_iter* = 2 shows wider spread of K_{DP} data for all Z_H values, although with slightly enhanced clustering of data around K_{DP}^{sc} for $Z_H \geq 35$ dBZ. These results indicate a trade-off between precision and accuracy when varying *windsize* and *n_iter* from 14 to 2. Particularly, larger settings favoring precision while deteriorating accuracy, and smaller settings favoring accuracy with deteriorated precision.

275 To further analyse the trade-off between accuracy and precision when varying *windsize* and *n_iter* in kdp_vulpiani, Fig. 7(a)-(b) show the NRMSE and normalized bias of K_{DP} estimates with varying *windsize* and *n_iter* as a function of Z_H. Figure 7(a) shows that *windsize* of 2 yielded the worst performance, implicating that the gain in accuracy by including fine-scale fluctuations in Φ_{DP} is not enough to compensate the increased errors due to the inclusion of outliers. On the other hand, *windsize* of 14 shows good performance across the entire Z_H range. However, the predominantly negative normalized bias of

280 *windsize* of 14 relative to smaller counterparts in Fig. 7(b) indicates that larger *windsize* leads to underestimation of K_{DP} more than lower *windsize* values. The consistent errors when varying *n_iter* in Fig. 7(a) indicate that this parameter setting does not impact as strongly as *windsize* in the performance of kdp_vulpiani, especially in low Z_H. However, results from Fig. 7(b) suggest that smaller *n_iter* significantly reduces the underestimation of K_{DP} estimates when *windsize* is large. Our results strongly resemble those reported in Reimel and Kumjian (2021), indicating that smaller number of iterations and

285 moderate window sizes significantly enhance the performance of kdp_vulpiani. Particularly, among the RMSE heat maps of kdp_vulpiani shown in Reimel and Kumjian (2021), *windsize* = 10 and *n_iter* = 2 produced the best results, coinciding with the smallest 35-50-dBZ-averaged NRMSE in this study.

3.1.3 Py-ART's Linear Programming method

Py-ART's implementation of an LP method proposed in Giangrande et al. (2013), phase_proc_lp, allows the user to tune

290 the window length for smoothing Φ_{DP}, *window_len*, and two intertwined parameters constraining the K_{DP} output via self-consistency relations: *self_const* and *coef*. The former is the weight of the self-consistency constraint and the latter is the
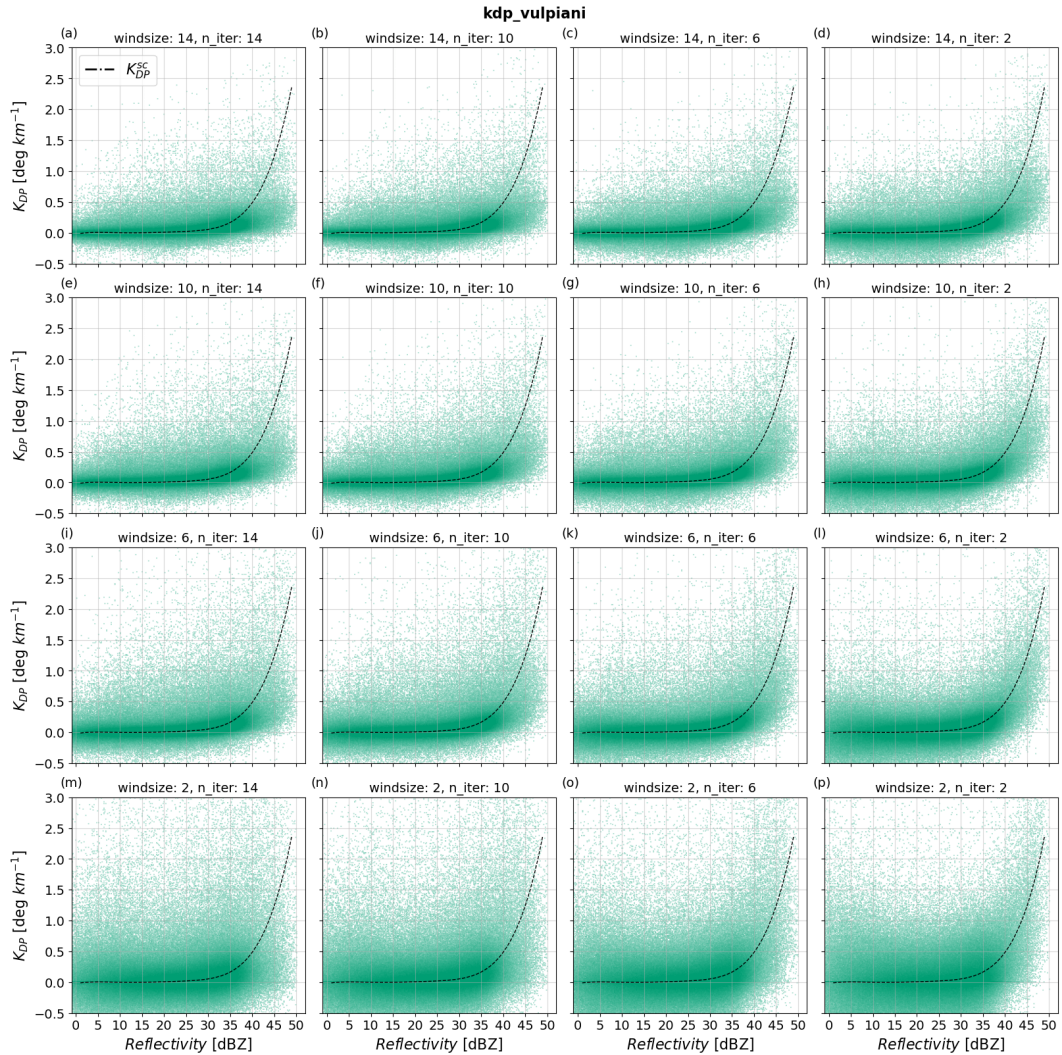
Figure 6. Scatter plots of estimated K_{DP} from kdp_vulpiani as function of reflectivity and for various values of $windsize$ and n_iter. The panels (a)-(p) show results with ($windsize$, n_iter) tuples values from (14, 14) to (2, 2), decreasing $windsize$ with increasing rows. The dashed black line corresponds to K_{DP}^{sc}.

exponent in the self-consistency relation linking K_{DP} to Z_H, given in Giangrande et al. (2013) as aZ_H^b but expressed in phase_proc_lp as $(10^{0.1 \times Z_H})^{coef}/self\_const$. Since information about the expected K_{DP} was known beforehand, given by K_{DP}^{sc}, we provided the method with the optimal values of *self_const* = 10^4 and *coef* = 0.914. In this way, the parameter optimization of phase_proc_lp was focused solely on *window_len* variations.

The parameter *window_len* defines the window length for smoothing the LP-processed Φ_{DP} field before K_{DP} is estimated.
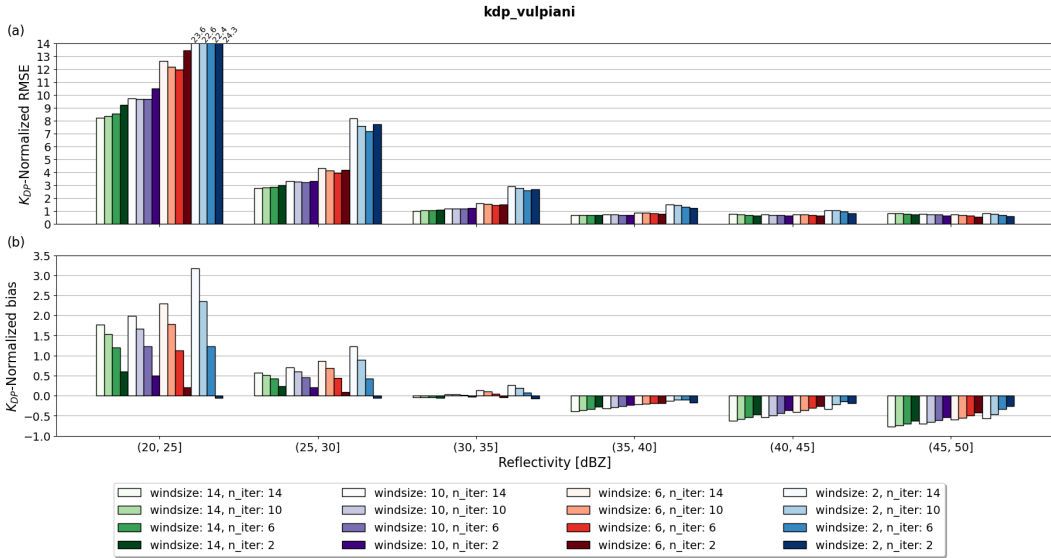
Figure 7. Panel (a) shows RMSE normalized by interval-averaged K_{DP}^{sc} of kdp_vulpiani relative to K_{DP}^{sc} as a function of reflectivity and for various values of $windsize$ and n_iter; panel (b) shows same as (a) but for the normalized bias metric.

The default setting of this parameter is 35, indicating a smoothing window length of 17.5 km for a range resolution of 500 m. To include finer-scale precipitation features (e.g. ∼2.5 km), phase_proc_lp was tested with $window\_len$ values ranging from 300 5 to 40. Figure 8(a)-(h) shows scatter plots comparing the performance of phase_proc_lp for different settings of $window\_len$ in estimating K_{DP}. Each panel from Fig. 8(a) to Fig. 8(h), shows K_{DP} estimated using window lengths from 5 to 40 in intervals of 5. The scatter plot from Fig. 8(a) with $window\_len = 5$ shows data points predominantly clustered around K_{DP}^{sc} across the entire Z_H range, indicating strong correlation between K_{DP} and K_{DP}^{sc}. Even in high Z_H ranges (i.e., ≥ 35 dBZ), the tight correlation between K_{DP} and K_{DP}^{sc} holds, indicating high accuracy and precision of K_{DP} in the presence of heavy 305 precipitation. The accuracy and precision of K_{DP} relative to K_{DP}^{sc} decreases progressively when $window\_len$ increases, indicated by the spreading and downward shifting of K_{DP} estimates relative to K_{DP}^{sc}. Especially for the range $Z_H \geq 35$ dBZ, the scatter plots from Fig. 8(e) to Fig. 8(h), with $windows\_len$ from 25 to 40, respectively, show substantial underestimation of K_{DP} relative to K_{DP}^{sc}, indicating stronger oversmoothing of Φ_{DP} for larger values of $window\_len$. Comparing the scatter plots, $window\_len = 5$ undoubtedly shows the best performance of phase_proc_lp. This result agrees with phase_proc_lp 310 $window\_len$ experiments by Li et al. (2023) in an extreme heavy precipitation event, where small $window\_len$ yielded the best performance. Compared to the phase_proc_lp experiments by Reimel and Kumjian (2021), our results suggest that smaller $window\_len$ produce overall more accurate K_{DP} estimates. However, the influence of the self-consistency constraints proposed in Giangrande et al. (2013) plays a key role in this aspect; if optimal self-consistency constraints are not provided or do not match theoretical expectations, the precision and accuracy in K_{DP} significantly reduces and larger $window\_len$ values 315 compensate this by oversmoothing Φ_{DP} (see Appendix A for results of the performance of phase_proc_lp with very little
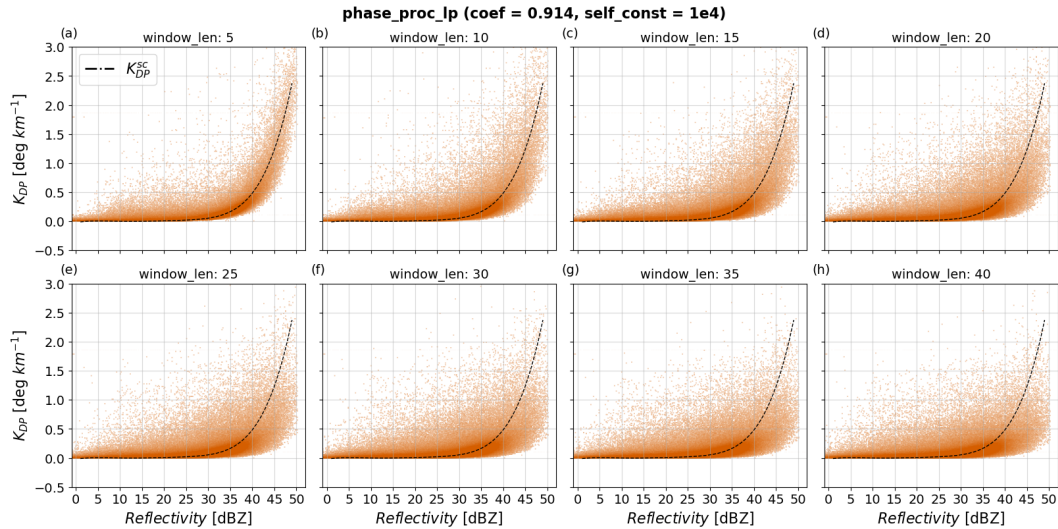
Figure 8. Scatter plots of estimated K_{DP} from phase_proc_lp as function of reflectivity and for various values of $window\_len$. The panels (a)-(h) show results with $window\_len$ values from 5 to 40, while fixing $coef$ to 0.914 and $self\_const$ to 10^4. The dashed black line corresponds to K_{DP}^{sc}.

influence of self-consistency constraints).

To investigate further the effects of $window\_len$ in the performance of phase_proc_lp, Fig. 9(a)-(b) show the NRMSE and normalized bias of K_{DP} estimates with varying $window\_len$ as function of Z_H. In agreement with the patterns observed in the 320 scatter plots from Fig. 8, $window\_len$ of 5 produced the best performance compared to other parameter settings. Interestingly, even in light precipitation (e.g. $Z_H <$30dBZ) smaller values of $window\_len$ produced the best NRMSE metrics, indicating that larger $window\_len$ do not further improve the precision of phase_proc_lp. Instead, larger $window\_len$ enhanced the bias of K_{DP} relative to K_{DP}^{sc} as shown in Fig. 9(b). The parameter $window\_len$ of 5 produced undoubtedly the best metrics for phase_proc_lp and it was selected as the optimal parameter.

325 ### 3.1.4 Wradlib's Vulpiani method

Wradlib's implementation of Vulpiani et al. (2012), kdp_from_phidp, features two optimizing parameters: *winlen* (number of gates used to reconstruct Φ_{DP}) and *dr* (gate length resolution in km). We tested *winlen* values from 3 to 11 and *dr* values from 0.5 to 4. Figure 10(a)-(l) shows scatter plots of K_{DP} estimates using kdp_from_phidp varying settings of *winlen* and *dr*. Each row of scatter plots holds *winlen* constant while decreasing *dr* from left to right. Similarly, each column of scatter plots 330 holds *dr* constant while decreasing *winlen* from top to bottom. The scatter plot from Fig. 10(a), with *winlen* = 11 and *dr* = 4, shows K_{DP} clustered predominantly around 0 deg km^{-1} across the entire Z_H range, indicating substantial oversmoothing of Φ_{DP}. Even for $Z_H \geq 30$ dBZ, the noticeable underestimation of K_{DP} relative to K_{DP}^{sc} indicates that kdp_from_phidp is not
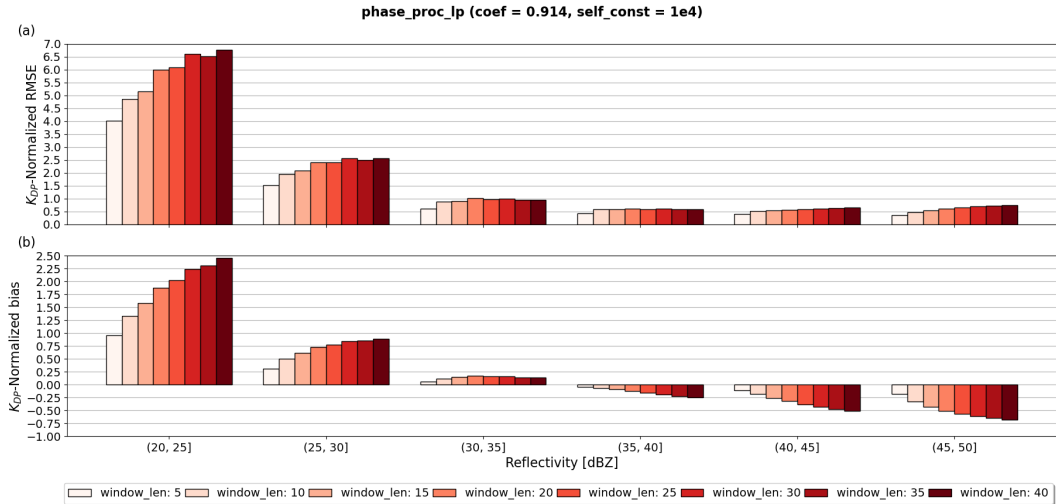
Figure 9. Panel (a) shows RMSE normalized by interval-averaged K_{DP}^{sc} of phase_proc_lp relative to K_{DP}^{sc} as a function of reflectivity and for various values of $window\_len$; panel (b) shows same as (a) but for the normalized bias metric.

able to capture signatures of heavy precipitation for large $winlen$ and dr settings. Moving towards the scatter plots from Fig. 10(d), a smaller dr enhances the accuracy of kdp_from_phidp, particularly for $Z_H \geq 30$ dBZ. However, the gain in accuracy
335 comes together with loss in precision in K_{DP} estimates, indicated by the wider spread of data. In addition, decreasing dr makes kdp_from_phidp more prone to the inclusion of outliers, illustrated by data points with $K_{DP} > 1$ deg km^{-1}, even for $Z_H \leq 20$ dBZ. The scatter plots from Fig. 10(e)-(h) follow the same behavior as in the first row except for wider spread of data, suggesting that decreasing $winlen$ while holding dr constant overall reduces the precision of kdp_from_phidp. When moving from Fig. 10(e) to Fig. 10(h), the accuracy of K_{DP} estimates increases while precision decreases when decreasing dr. In the
340 last row, i.e., from Fig. 10(i) to Fig. 10(l), K_{DP} estimates are the most scattered for the same dr, indicating loss in precision of kdp_from_phidp when reducing $winlen$. The scatter plot from Fig. 10(l) with the smallest parameter settings tested ($winlen = 3$ and $dr = 0.5$) resembles a scatter plot of random noise with no significant clustering of data, and suggesting extremely poor correlation relative to K_{DP}^{sc}. Comparing the scatter plots row-wise and column-wise, decreasing $winlen$ or dr significantly deteriorates the precision of the method. However, the effect on the accuracy is more complex; simultaneous setting of $winlen$
345 and dr to large values lead to substantial underestimation of K_{DP}, whereas small values lead to noisy K_{DP}, respectively. These results suggest that the effects of varying $winlen$ and dr in the performance of kdp_from_phidp are strongly intertwined, requiring more analysis in the trade-off between accuracy and precision offered by variations of these parameters.

To analyse the trade-off between accuracy and precision when $winlen$ and dr in kdp_from_phidp, Fig. 11(a)-(b) show the
350 NRMSE and normalized bias of K_{DP} estimates with varying $winlen$ and dr as function of Z_H. Even though Fig. 11(a) has been clipped at 5.0, it is important to notice the significantly high values when using the smallest dr (97.6, 135.4 and 278.6 for $winlen$ of 11, 7, and 3, respectively). The predominantly higher NRMSE values with the smallest dr indicate that the
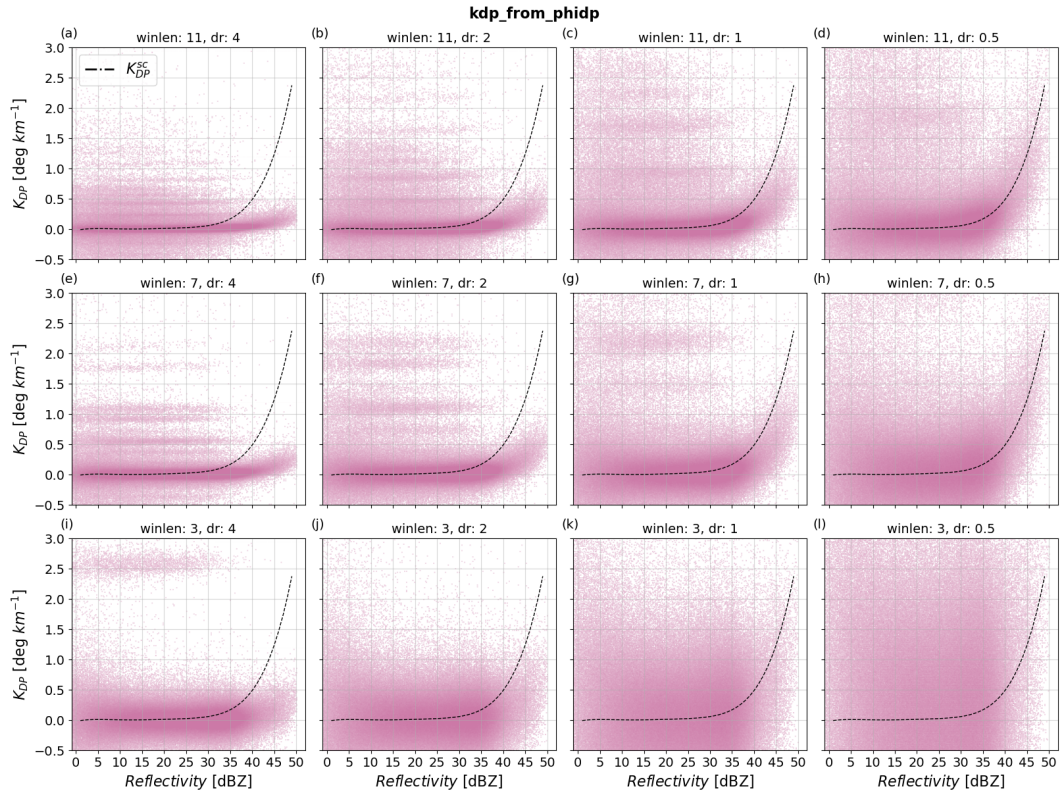
Figure 10. Scatter plots of estimated K_{DP} from kdp_from_phidp as function of reflectivity and for various values of $winlen$ and dr. The panels (a)-(l) show results with ($winlen$, dr) tuples values from (11, 4) to (3, 0.5); $winlen$ decreases in intervals of 4 per row whereas dr decreases by half per column. The dashed black line corresponds to K_{DP}^{sc}.

precision of kdp_from_phidp reduces significantly with $dr < 1$ for any $winlen$ tested. An exception occurs in the Z_H interval $(45, 50]$ dBZ, where the smallest dr yield the best metrics due to slight improvements in the accuracy. Despite the limited amount of data within this Z_H interval (see Fig. 3), the clustering of K_{DP} around K_{DP}^{sc} in Fig. 10 and the small normalized biases in Fig. 11(b) suggest that accuracy improved slightly for the smallest dr. The smaller NRMSE with high dr in Fig. 11(a) is counterbalanced by the predominantly larger negative bias for larger dr in Fig. 11(b). This implies that larger dr values in kdp_from_phidp lead to underestimation of K_{DP} for all $winlen$ tested. As a conclusion, combining large $winlen$ with smaller dr produces best performance in heavier precipitation (i.e., $Z_H > 30$ dBZ), whereas combining large $winlen$ with larger dr produces best results for light precipitation. Overall, small values of $winlen$ reduces significantly the precision in the method without improving accuracy. The parameter setting with the smallest 35-50-dBZ-averaged NRMSE was $winlen = 11$ and $dr = 2$.
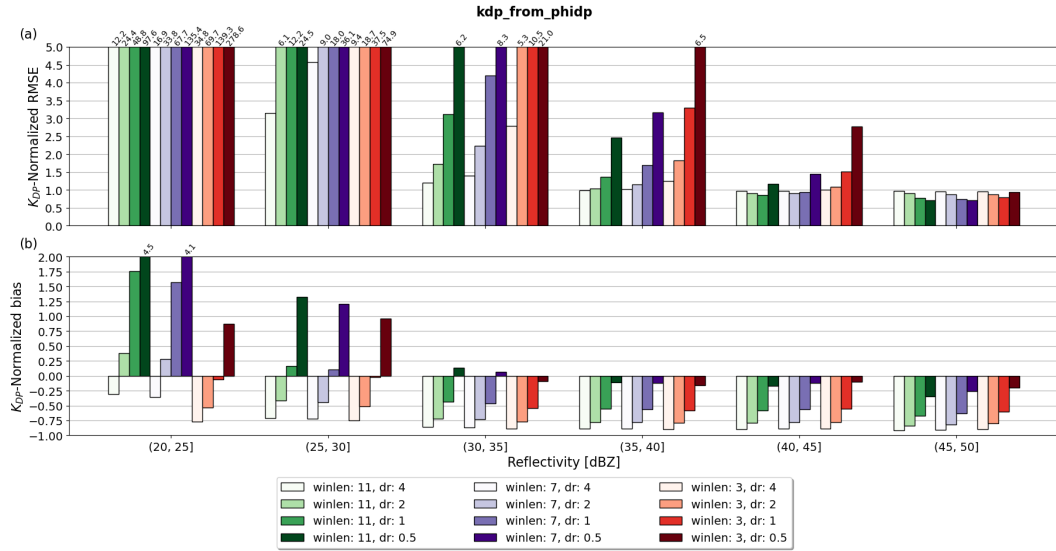
Figure 11. Panel (a) shows RMSE normalized by interval-averaged K_{DP}^{sc} of kdp_from_phidp relative to K_{DP}^{sc} as a function of reflectivity and for various values of $winlen$ and dr; panel (b) shows same as (a) but for the normalized bias metric. The numbers on top of the bars indicate the values of the metric exceeding the y-axis limit selected

3.2 Performance Assessment of Methods Relative to K_{DP}^{sc}

The performance of the methods is analyzed qualitatively in Sec. 3.2.1 and quantitatively in Sec. 3.2.2. For these analyses, we used the parameter-optimized kdp_maesaka, kdp_vulpiani, phase_proc_lp and kdp_from_phidp, and included kdp_schneebeli and kdp_iris.

3.2.1 Qualitative Assessment

We qualitatively assessed the precision and accuracy of the estimated K_{DP} using scatter plots of K_{DP} vs. Z_H for each method. Figure 12 shows six scatter plots comparing the performance of kdp_maesaka, kdp_vulpiani, phase_proc_lp, kdp_from_phidp, kdp_schneebeli and kdp_iris in estimating K_{DP}. Each scatter plot illustrate the relationship between estimated K_{DP} (y-axis) relative to Z_H (x-axis), against benchmarking K_{DP}^{sc} (black dashed line). For the parameter-optimized methods in Figs. 12(a)-(d), the optimal parameter selected is indicated in the plot's title together with the method's name. Comparing the scatter plots, phase_proc_lp demonstrates the highest accuracy and precision, evidenced by the data narrowly clustered around K_{DP}^{sc} across the entire Z_H range. Methods kdp_from_phidp and kdp_schneebeli show the least accuracy and precision, with broader spread and more outliers, particularly when $Z_H < 30$ dBZ. For higher Z_H values, even though kdp_from_phidp shows better precision but worse accuracy than kdp_schneebeli, these two methods strongly underestimate K_{DP}, evidenced by the predominant clustering of K_{DP} estimates below 0.5 deg km^{-1}. Method kdp_maesaka shows less scattering of K_{DP} estimates compared to kdp_from_phidp and kdp_schneebeli, indicating higher precision and accuracy particularly for $Z_H < 30$ dBZ.

However, for $Z_H \geq 30$ dBZ, the performance of kdp_maesaka deteriorates rapidly, as shown by the broader spread and significant underestimation of K_{DP} relative to K_{DP}^{sc}. Methods kdp_vulpiani and kdp_iris show moderate performance, with better accuracy and precision than kdp_from_phidp, kdp_schneebeli and kdp_maesaka, but less than phase_proc_lp. Between methods kdp_vulpiani and kdp_iris, kdp_vulpiani shows better correlation of K_{DP} estimates with K_{DP}^{sc} for $Z_H \geq 35$ dBZ, indicating higher accuracy in heavier precipitation. However, kdp_iris shows less scattering across the entire Z_H range, indicating overall higher precision than kdp_vulpiani. Methods kdp_vulpiani, kdp_from_phidp, kdp_schneebeli and kdp_iris include negative K_{DP} values, which should not be expected in rain observations. These negative estimates show up predominantly in lighter precipitation (i.e., $Z_H < 30$ dBZ), indicating they are most likely produced by noise in Φ_{DP}. However, the inclusion of negative K_{DP} estimates are useful, for instance, in the detection of snow crystals, allowing kdp_vulpiani, kdp_from_phidp, kdp_schneebeli and kdp_iris to be used in a wider range of applications when compared to kdp_maesaka and phase_proc_lp. The relatively high accuracy and precision of kdp_iris and kdp_vulpiani, together with the inclusion of negative K_{DP} estimates, leave these two methods as well-suited candidates for QPE, calibration and hydrometeor classification routines.

3.2.2 Quantitative Assessment

The quantitative assessment of the methods was achieved throughout the metrics NRMSE and normalized bias, and complemented with statistics from the Wasserstein distance (WD) (Ramdas et al., 2015). The WD measures the similarity between two cumulative distributions, given in this study by K_{DP} estimated by each method, and K_{DP}^{sc}. On the one hand, NRMSE and normalized bias computed as a function of Z_H, allows the assessment of relative accuracy and precision of the methods based on precipitation intensities. The WD, on the other hand, estimated independently from each radar scan and with statistics over the entire set of scans, allows the assessment of the relative consistency and robustness of the methods.

Figures 13(a)-(b) show NRMSE and normalized bias of estimated K_{DP} for each method. Overall, phase_proc_lp shows the best performance, as evidenced by the lowest NRMSE values in Fig. 13(a) and moderately low bias in Fig. 13(b) across all Z_H intervals. In contrast, kdp_schneebeli shows the worst performance among the methods, indicated by the highest NRMSE values and moderately high bias across all Z_H intervals. Method kdp_from_phidp shows substantially higher NRMSE values than kdp_maesaka, kdp_vulpiani, phase_proc_lp and kdp_iris but significantly smaller than kdp_schneebeli, particularly for the smallest Z_H values. The relatively small bias of kdp_from_phidp when NRMSE values are substantially high, is explained by the positive-to-negative symmetrical spread of K_{DP} estimates around the x-axis, indicating poor precision. Additionally, the persistent negative and large normalized bias of this method relative to the other methods indicates kdp_from_phidp underestimates K_{DP} the most. Methods kdp_maesaka, kdp_vulpiani and kdp_iris have moderate NRMSE values, performing better than kdp_schneebeli and kdp_from_phidp but not as well as phase_proc_lp. Among these three methods, kdp_maesaka has the smallest NRMSE values for $Z_H \leq 35$ dBZ but the largest when $Z_H \geq 40$ dBZ. The relatively large positive bias of kdp_maesaka when $Z_H < 30$ is a direct consequence of the exclusion of negative K_{DP} estimates. However, the persistent larger negative bias of kdp_maesaka relative to kdp_vulpiani and kdp_iris when $Z_H \geq 30$ dBZ, indicates stronger underestimation of K_{DP} and thus lesser accuracy. These results indicate that, in comparison to others, kdp_maesaka performs slightly
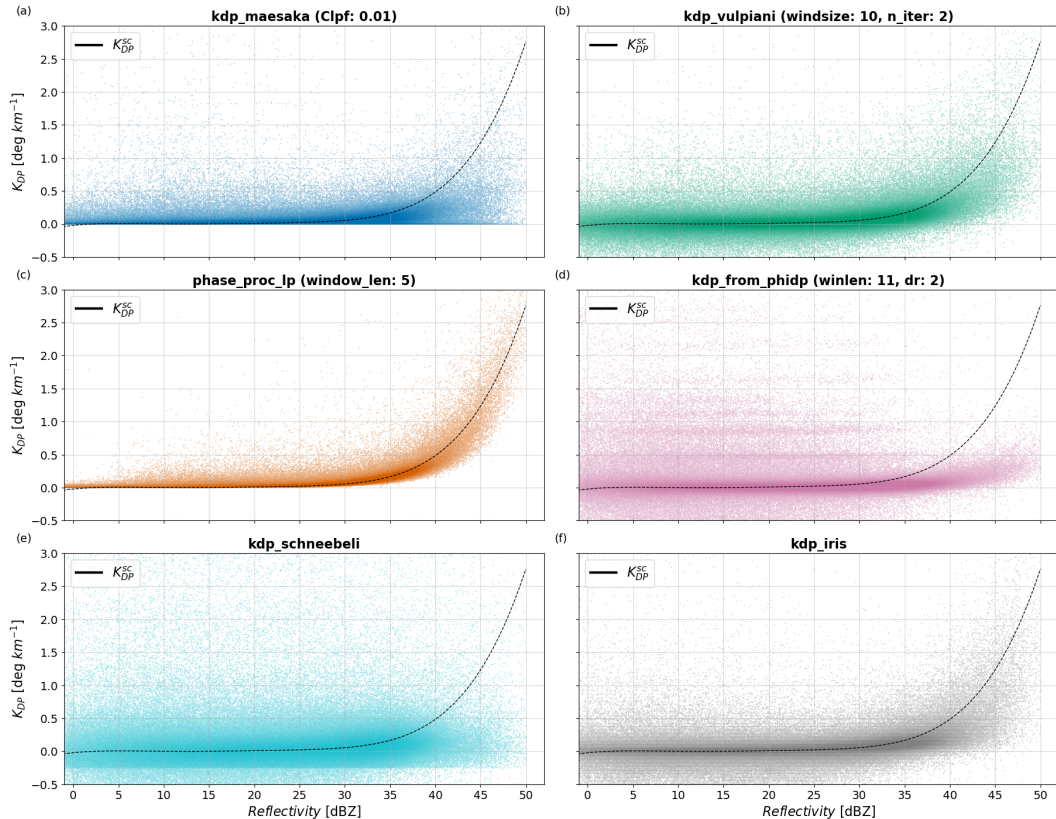
Figure 12. Scatter plot of estimated K_{DP} from each parameter-optimized method relative to K_{DP}^{sc} as function of reflectivity. Panels (a)-(f) show kdp_maesaka, kdp_vulpiani, kdp_iris, phase_proc_lp, *kdp_from_phi_dp* and kdp_schneebeli, respectively. The dashed black line corresponds to K_{DP}^{sc}.

better in light precipitation (i.e., $Z_H < 30$ dBZ) but worse in heavier precipitation. Between kdp_vulpiani and kdp_iris, kdp_iris shows overall smaller NRMSE and normalized bias, indicating higher accuracy and precision than kdp_vulpiani.

415   Complementary to NRMSE and normalized bias metrics, we evaluated the consistency and robustness of the methods using the Wasserstein distance (WD). The WD was computed for each radar scan independently using the *wasserstein_distance* module from SciPy (Virtanen et al., 2020). Then, the statistics from the estimated WD values for all scans were visualized and analysed using boxplots. Figure 14 consists of two panels comparing the WD boxplots of the methods. Figure 14(a) compares the WD for all methods, including kdp_schneebeli, which presented significantly large WD. Figure 14(b) presents the same

420   data as (a) but excluding kdp_schneebeli to better compare the remaining methods. Each boxplot summarizes the statistics of estimated WD by showing the median (black dashed line), interquartile ranges (IQR), $1.5\times$ the IQR (whiskers) and outliers (crosses). The insights provided by boxplots in this analysis are twofold. First, a WD median closer to 0 indicates higher similarity between the cumulative distributions of a method's estimated K_{DP} and that from K_{DP}^{sc}, ultimately indicating higher accuracy. Second, a narrower IQR indicates less variability of a method's performance between scans, indicating higher con-
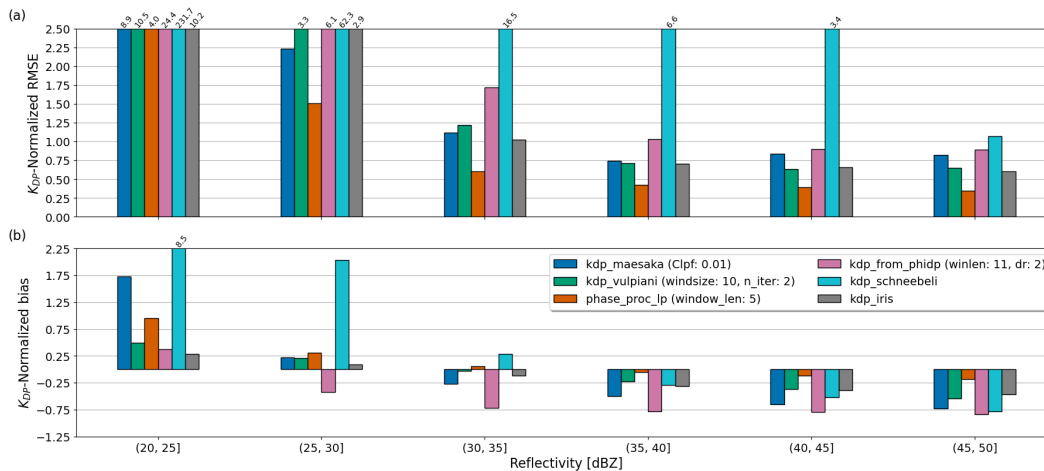
Figure 13. Panel (a) shows bias of estimated K_{DP} from each parameter-optimized method relative to K_{DP}^{sc} as function of reflectivity; panel (b) shows same as (a) but bias normalized by interval-averaged K_{DP}^{sc}. The numbers on top of the bars indicate the values of the metric exceeding the y-axis limit selected

sistency.

In Figure 14(a), the x-axis lists six methods: kdp_maesaka, kdp_vulpiani, phase_proc_lp, kdp_from_phidp, kdp_schneebeli and kdp_iris. The y-axis measures the WD values, ranging from 0 to 2. The boxplot for method kdp_schneebeli shows the largest WD with a median of 0.33, an IQR from 0.18 to 0.45, and several outliers. The other methods (kdp_maesaka, kdp_vulpiani, phase_proc_lp, kdp_from_phidp and kdp_iris) have median WD values ranging from 0.0 to 0.1, with smaller IQRs and fewer outliers. In Figure 14(b), method kdp_schneebeli is excluded, allowing for a clearer comparison of methods kdp_maesaka, kdp_vulpiani, phase_proc_lp, kdp_from_phidp and kdp_iris. The y-axis is rescaled to range from 0.0 to 0.2 for better visualization. Method phase_proc_lp has the lowest WD median at 0.01 with a narrow IQR from 0.008 to 0.018. Method kdp_from_phidp has significantly larger WD median of 0.098 and IQR from 0.077 to 0.122. Methods kdp_maesaka and kdp_iris have WD medians of 0.026 and 0.041, respectively, with moderate IQR and few outliers. Method kdp_vulpiani has a moderate WD median of 0.049 but noticeably wider IQR from 0.033 to 0.096 when compared to kdp_maesaka, phase_proc_lp, kdp_from_phidp and kdp_iris.

The large WD median of kdp_schneebeli indicates it performs worse compared to the other methods, overshadowing the performance difference among the remaining methods. Additionally, the large IQR of kdp_schneebeli implies that the method does not perform consistently thus reducing its reliability. Method phase_proc_lp demonstrates the best and consistent performance with the lowest WD median and narrowest IQR. These results additionally indicate that the distribution of K_{DP} estimated from phase_proc_lp is the closest to K_{DP}^{sc}. It is important to remember here that phase_proc_lp is supported by self-consistency re-
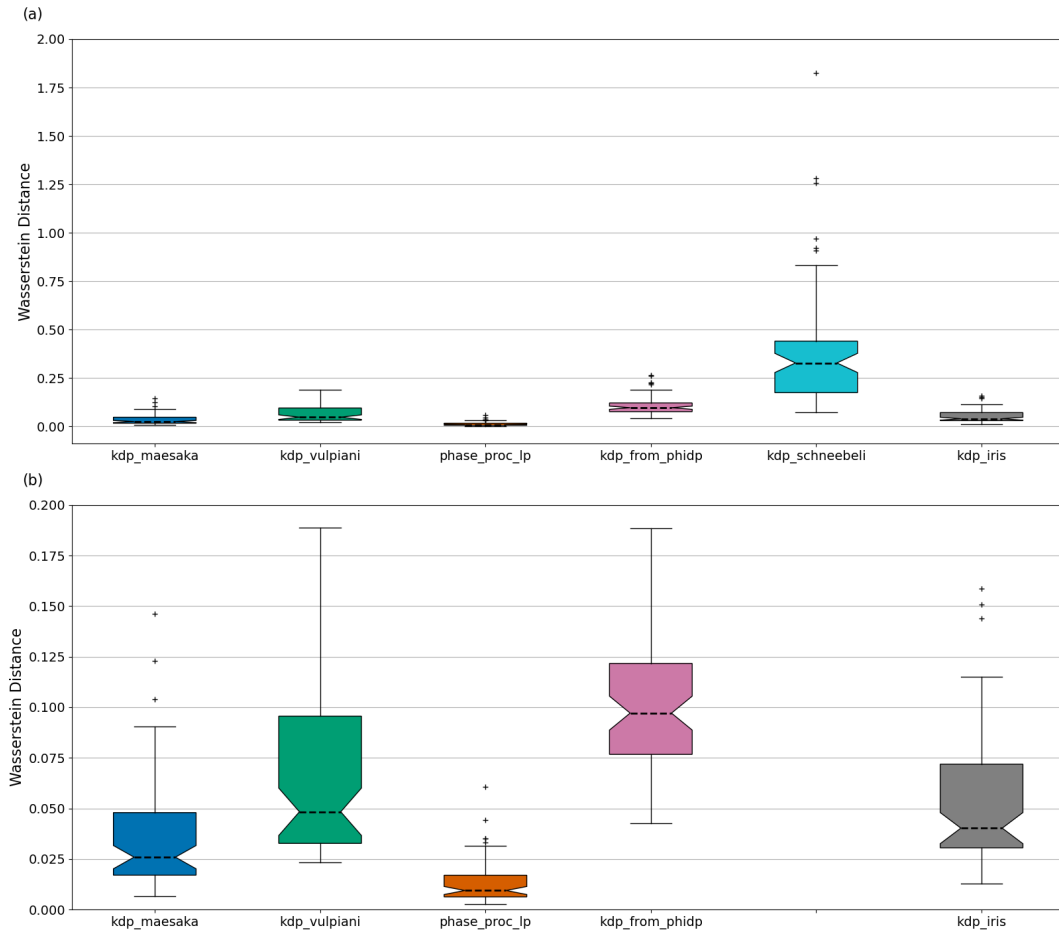
Figure 14. Panel (a) shows the boxplot of computed WD for each parameter-optimized method; panel (b) shows same as (a) but excluding kdp_schneebeli for better visualization of the outperforming methods. The boxplot displays the WD median (black dashed line), IQRs (boundaries of the box), $1.5\times$ the IQR (whiskers) and the outliers (black crosses).

lations constraining K_{DP} estimates based on Z_H observations, ultimately enhancing its accuracy and stability. The moderate
445   IQR and significantly larger WD median of kdp_from_phidp, indicate its performance is consistent albeit less accurate relative to the other methods. Method kdp_vulpiani in turn, has a moderate WD median but relatively larger IQR, indicating better accuracy than kdp_from_phidp although less consistent. Methods kdp_maesaka and kdp_iris show similar consistency and accuracy, evidenced by their relatively low WD medians and moderate IQRs. These findings suggest that while kdp_schneebeli is the less accurate and consistent, the performance among the remaining methods vary, with phase_proc_lp presenting the
450   highest robustness provided the method with quality-controlled Z_H and optimized self-consistency settings.

3.3 Consistency Analysis of K_{DP} Retrievals

Each method has its unique combination of mathematical approach, data requirements, and constraints (see Table 1), indicating uniqueness in the K_{DP} fields produced. How similar or dissimilar are these outputs is not clearly visible from the metrics computed nor the scatter plots displayed in Sec. 3.2. To answer this question, we study the consistency among methods using

455   K_{DP} vs K_{DP} correlation plots shown in Fig. 15. Each scatter plot in Fig. 15 shows the relationship between K_{DP} estimated by a method (y-axis) with respect to K_{DP} estimated from a different method (x-axis) and the Pearson correlation coefficient (R) is shown in the upper left corner of each scatter plot. The axes range from -0.5 to 3.0 deg km^{-1} to include negative K_{DP} estimates. This part of the analysis does not require any ground-truth framework, allowing the use the entirety of radar dataset, i.e., including the attenuated observations (see red data in Fig. 3).

460

In Figure 15, the scatter plot of kdp_iris against kdp_vulpiani shows the best correlation among the methods, illustrated by the data significantly clustered along the diagonal and corroborated by the highest R of 0.66. Methods kdp_iris and kdp_vulpiani correlate similarly to phase_proc_lp, indicated by the second highest R of 0.65 for both. In relation to kdp_maesaka, the consistencies of kdp_iris and kdp_vulpiani are rather moderate, whereas in relation to kdp_from_phidp and kdp_schneebeli, they

465   are significantly poorer. Among the methods, kdp_schneebeli correlates the least with any of the methods, evidenced by the data widely spread along the axes and showing negligible clustering of data along the diagonal. Particularly kdp_schneebeli against kdp_from_phidp shows the worst consistency with $R = 0$ and the majority of data clustered around the x- and y-axis. Method phase_proc_lp correlates moderately to kdp_maesaka with an $R = 0.41$, although the scatter plot does not exhibit any particular pattern or clustering of data along the diagonal. Relative to kdp_from_phidp, phase_proc_lp shows significantly

470   lower R despite the clear data correlation off of the diagonal. However, the small R value becomes evident when observing the dense clustering of data around 0 deg km^{-1} for phase_proc_lp. This results indicates the consistency between kdp_from_phidp and phase_proc_lp is highly influenced by the negative K_{DP} estimates in kdp_from_phidp that are mapped to 0 deg km^{-1} in phase_proc_lp. Overall, the scatter plots show that kdp_from_phidp underestimates K_{DP} relative to the other methods. Method kdp_maesaka shows no significant correlation with any method, with the largest R being 0.41 relative to both phase_proc_lp

475   and kdp_vulpiani.

4   Conclusions

In this study, we conducted a comprehensive evaluation of several K_{DP} estimation methods using C-band weather radar data, with a focus on their performance in rainfall observations. We employed a self-consistency framework, that links Z_H and Z_{dr} observations with K_{DP}, as the basis for our evaluations. This approach allows for the construction of the reference K_{DP}

480   observations that can be used to assess the accuracy and robustness of the studied K_{DP} estimation methods. The use of the self-consistency framework requires rather strict quality control which is described in the paper. In this way, our study focuses on the performance of the methods in highly idealized rainfall observations.
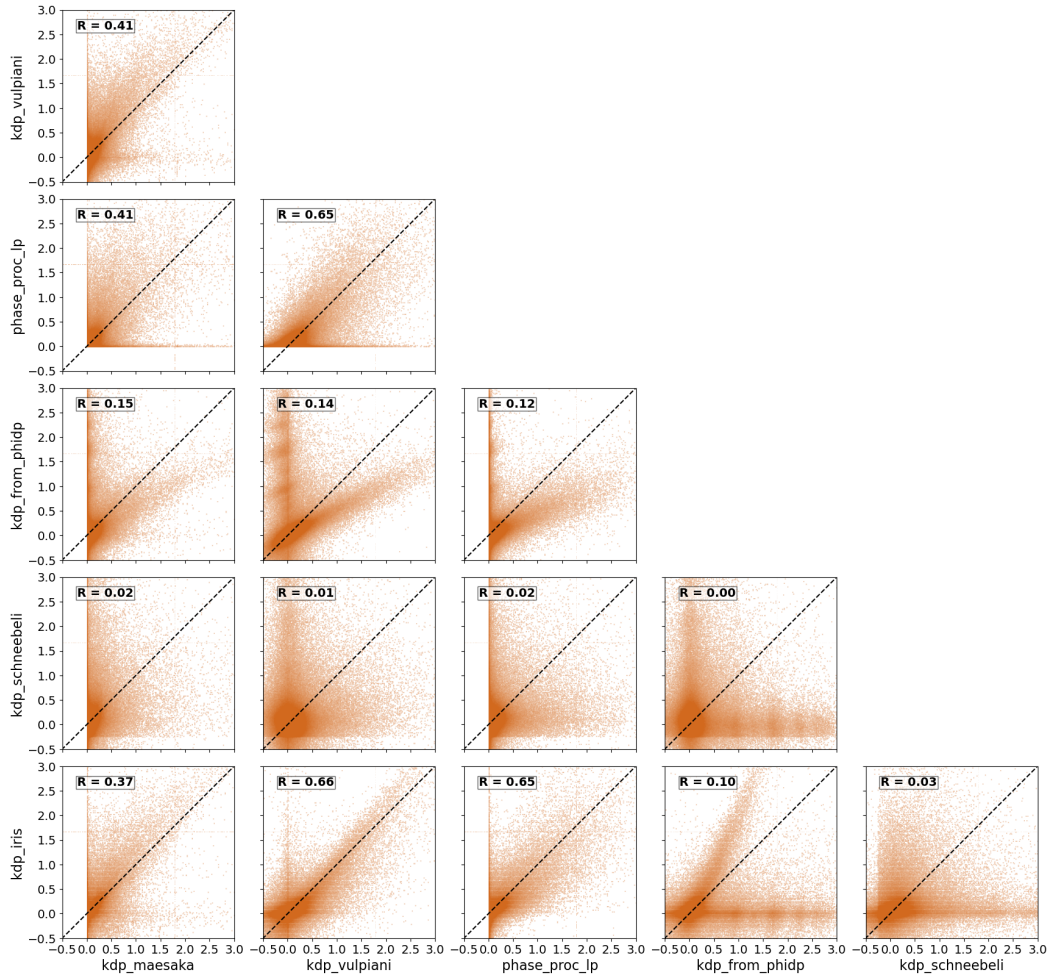
Figure 15. Correlation between the K_{DP} estimation methods. Each scatter plot shows the relationship between two different methods without repetition and no method is compared to itself. The x- and y-axis represent K_{DP} estimated by a method in units of deg km^{-1}. Each plot shows the Pearson correlation coefficient between the two compared methods.

Some, four out of six, of the K_{DP} estimation methods have user-configurable parameters. Using the proposed evaluation framework we could define optimized parameter settings. Most of the methods showed significant improvement in the performance after the optimization.

By comparing the relative performances of the estimation methods over the range of rain intensities, as characterized by the radar Z_H values, we have found significant difference in performances of the evaluated methods. Overall, implementations of Giangrande et al. (2013), Vulpiani et al. (2012) and Wang and Chandrasekar (2009) exhibited the lowest NRMSE and normalized biases over the studied range, from 20 to 50 dBZ of Z_H values.

Our comparative analysis revealed that while the implementation of Giangrande et al. (2013)'s method stands out for its high accuracy and precision, its performance is heavily dependent on the provided self-consistency constraint. Without proper optimization of the self-consistency relation, linking Z_H and K_{DP}, and quality control of Z_H, even the best window length setting for this method can lead to suboptimal results, i.e. higher RMSE and K_{DP} underestimation at higher Z_H values. It should be noted, however, that the reference framework and Giangrande et al. (2013)'s method use self-consistency relations to determine K_{DP}, and therefore, the uncertainties are correlated and part of the reported performance is caused by this dependence. Implementations of Vulpiani et al. (2012) and Wang and Chandrasekar (2009) showed good performance and do not require use of other radar variables, which potentially make them less sensitive to radar data quality issues, such as calibration and attenuation.

An additional qualitative comparison of the methods performances was carried out by computing correlations of derived K_{DP} values from the dataset that also included attenuated radar observations. The correlation between K_{DP} values estimated using different methods is not very high. The highest correlation values of 0.65-0.66 were observed between Giangrande et al. (2013), Vulpiani et al. (2012) and Wang and Chandrasekar (2009) methods. This indicates that uncertainty between different precipitation estimates could stem from the differences in the used K_{DP} methods.

The study is based on the self-consistency framework that limits it to the cases where no significant attenuation is observed. Additionally, the scope of our study is limited to the Finnish climatology and a single radar frequency, namely C-band radar observations. Despite these limitations, our findings offer valuable guidance for the use of K_{DP} estimation methods in rainfall observations. These results have significant implications for both operational radar network and hydrometeorological research, where the accuracy, precision, and stability of K_{DP} estimates are crucial.

Appendix A: Influence of self-consistency constraint in *phase_proc_lp*

Figure A1 shows same scatter plots as in Fig. 8, with K_{DP} estimated from phase_proc_lp using $self\_const$ of 10^6 instead of 10^4. The motivation behind was to study the performance of phase_proc_lp with little influence of self-consistency constraints. In Giangrande et al. (2013), the non-negativity condition in K_{DP} estimates is ensured by restricting the b-vectors: $\boldsymbol{b} \geq 0$. In addition, to produce more realistic K_{DP} estimates, they introduced the self-consistency relation $K_{DP}(Z_H) = aZ_H^b$ to bound the estimates based on observed Z_H, requiring that the user provides quality controlled data. The restriction of the b-vectors becomes $\boldsymbol{b} \geq aZ_H^b$, which in phase_proc_lp is implemented as $\boldsymbol{b} \geq (10^{0.1 \times Z_H})^{coef}/self\_const$. Therefore, a two order of magnitudes larger $self\_const$ value was used in this study to test the performance of phase_proc_lp with a significantly reduced influence of self-consistency constraints. The scatter plots show K_{DP} data clustered around K_{DP}^{sc} up to 35 dBZ. Beyond this threshold, precision and accuracy decays significantly regardless of the window length. However, in scatter plots with larger window lengths K_{DP} data is less scattered across the entire Z_H range and only slightly less accurate after 35 dBZ.
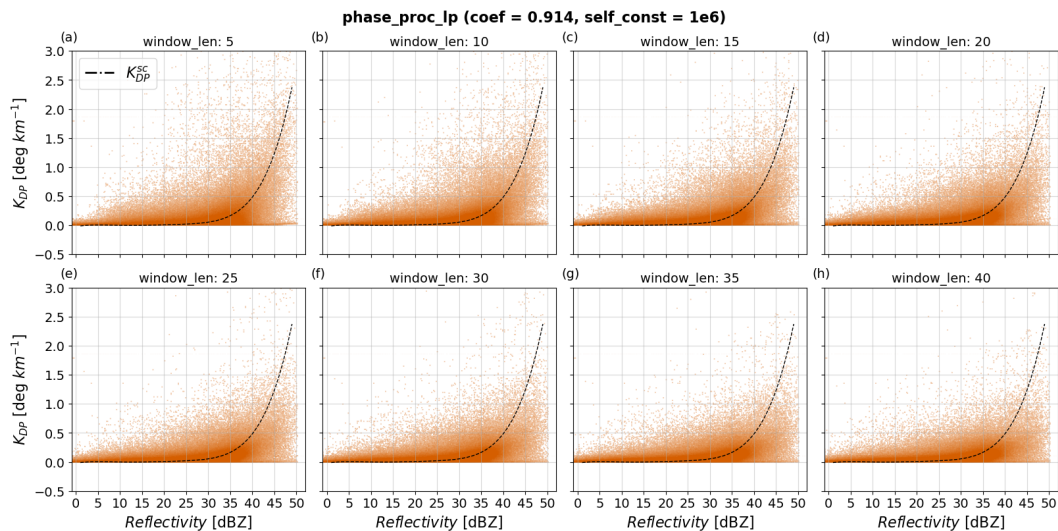
Figure A1. Scatter plots of estimated K_{DP} from phase_proc_lp as function of reflectivity and for various values of $window\_len$. Panels (a)-(h) show results with $window\_len$ values from 5 to 40, while fixing $coef$ to 0.914 and $self\_const$ to 10^6. The solid black line denotes corresponds to K_{DP}^{sc}.

525

To further investigate the effects of the self-consistency constraint in phase_proc_lp, Fig. A2(a)-(b) show the normalized RMSE and bias of K_{DP} (estimated with $self\_const = 10^6$) relative to K_{DP}^{sc}. Interestingly, the normalized RMSE in Fig. A2(a) behaves inversely as in normalized RMSE in Fig. 9, whereas normalized bias shows similar behavior for both. The opposite behaviors in normalized RMSE results indicate that window length has a strong impact in the performance of phase_proc_lp

530 depending on whether the adequate self-consistency settings were provided; if so, smaller window lengths yield better performance by capturing fine scale precipitation features specially in heavy precipitation. In the opposite case, larger window lengths yield better performance by oversmoothing Φ_{DP} thus reducing the impact of noise at the expense of loosing fine-scale precipitation features. The oversmoothing effect from larger window lengths in K_{DP} is also implied from the normalized bias shown in Fig. A2(b); larger window lengths produced absolute largest biases in both extremes of the Z_H range. In addition, even

535 though the normalized bias shows similar behavior for $self\_const = 10^6$ and $self\_const = 10^4$, the latter produces larger differences between window lengths, indicating that high accuracy and precision of phase_proc_lp predominates in smaller window lengths, provided the adequate self-consistency constraints and quality-controlled Z_H.
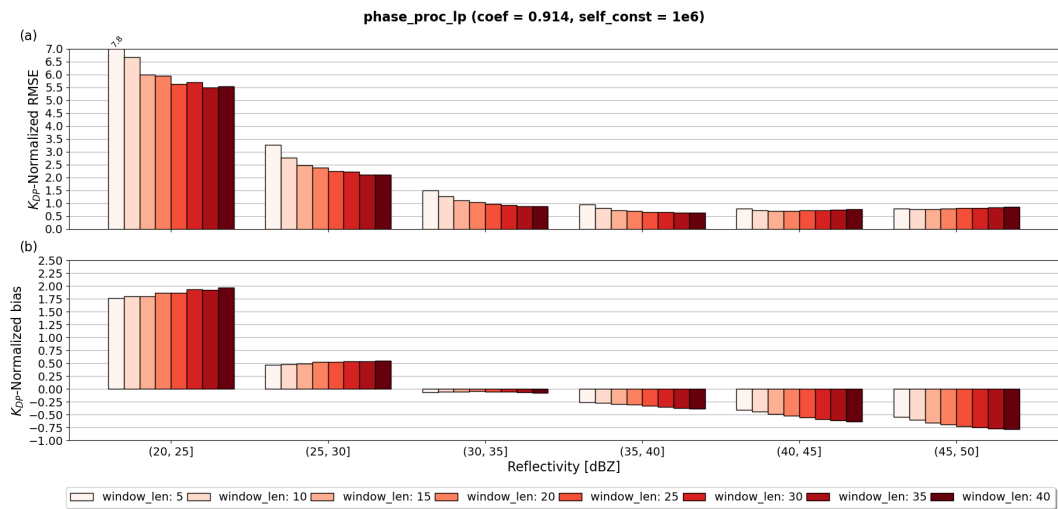
Figure A2. Panel (a) shows RMSE normalized by interval-averaged K_{DP}^{sc} of phase_proc_lp relative to K_{DP}^{sc} as a function of reflectivity and for various values of $window\_len$; panel (b) shows same as (a) but for the normalized bias metric.

Data Availability

The radar raw data and KDP dataset, accessed via the link in Aldana (2024), includes the raw radar data and KDP processed
540 data used to analyse the KDP estimation methods. The data has been processed using Python and it includes:

- The folder "radar" includes several subfolders: "yyyy/mm/dd/iris/raw/VAN". The "VAN" subfolder includes the .raw
  radar with PPI's observed by Vantaa radar at an elevation angle of 0.7 for a specific time: "yyyymmddHHMM_VAN.PPI3_B.raw".
  This data can be further read with Py-ART (Helmus and Collis, 2016).

- The folder "KDP_data" includes 5 .hdf5 files storing tables containing information about date (in pandas numerical
545 value. It requires transformation to datetime object), Z (in dBZ), Zdr (in dB), attenuated gate (as boolean), theoretical
  or self-consistency KDP (in deg / km) and computed KDP (in deg / km) from a given method for different settings. The
  method is indicated in the name of the file as kdp_method_scatter.hdf5, where method can be:

  - 'iris_sch', referring to table containing KDP from iris software (used in the Finnish Meteorological Institute) and
    KDP computed from Py-ART's implementation of Schneebeli et al. (2014). These two methods were computed
550 together because only one KDP output was retrieved. They do not feature any user-configurable parameters to test.

  - 'mae', referring to table containing KDP computed from Py-ART's implementation of Maesaka et al. (2012). The
    columns correspond to KDP computed by varying parameter 'Clpf'.

  - 'vulpiani', referring to table containing KDP computed from Py-ART's implementation of Vulpiani et al. (2012).
    The columns correspond to KDP computed by varying parameters 'windsize' and 'n_iter'.

555 - 'pplp', referring to table containing KDP computed from Py-ART's implementation of Giangrande et al. (2013).
    The columns correspond to KDP computed by varying parameter 'windowlen'.

  - 'wradlib', referring to table containing KDP computed from Wradlib's implementation of Vulpiani et al. (2012).
    The columns correspond to KDP computed by varying parameters 'winlen' and 'dr'.

The disdrometer dataset to obtain the DSD parameters and be accessed via the link provided in Moisseev (2024).

560 **Author Contributions**

MA conducted the investigation process, collected the data, performed the formal analysis of the data and visualization; MA,
SP and DM designed the methodology; SP, AL, MK and DM formulated the research goals and aims; AL and DM provided
data; MA prepared the manuscript draft; MA, SP, AL, MK and DM reviewed, commented and edited the manuscript.

Competing Interests

565 The contact author has declared that none of the authors has any competing interests

Acknowledgements

We thank Jenna Ritvanen for her valuable comments for improving the visualization of the data; we thank colleagues from the Early Career Community at the Finnish Meteorological Institute for feedback on how to make the manuscript reachable also for general audience.

References

Al-Sakka, H., Boumahmoud, A.-A., Fradon, B., Frasier, S. J., and Tabary, P.: A New Fuzzy Logic Hydrometeor Classification Scheme Applied to the French X-, C-, and S-Band Polarimetric Radars, Journal of Applied Meteorology and Climatology, 52, 2328–2344, https://doi.org/10.1175/JAMC-D-12-0236.1, 2013.

Aldana, M.: Raw radar data and KDP dataset, https://doi.org/10.57707/fmi-b2share.4126c5db27d24ddeae10d5c3163ff95a, 2024.

Andrić, J., Kumjian, M. R., Zrnić, D. S., Straka, J. M., and Melnikov, V. M.: Polarimetric Signatures above the Melting Layer in Winter Storms: An Observational and Modeling Study, Journal of Applied Meteorology and Climatology, 52, 682–700, https://doi.org/10.1175/JAMC-D-12-028.1, 2013.

Aydin, K. and Giridhar, V.: C-Band Dual-Polarization Radar Observables in Rain, Journal of Atmospheric and Oceanic Technology, 9, 383–390, https://doi.org/10.1175/1520-0426(1992)009<0383:CBDPRO>2.0.CO;2, 1992.

Aydin, K., Direskeneli, H., and Seliga, T.: Dual-Polarzation Radar Estimation of Rainfall Parameters Compared with Ground-Based Disdrometer Measurements: October 29, 1982 Central Illinois Expenment, IEEE Transactions on Geoscience and Remote Sensing, GE-25, 834–844, https://doi.org/10.1109/TGRS.1987.289755, 1987.

Bechini, R. and Chandrasekar, V.: A Semisupervised Robust Hydrometeor Classification Method for Dual-Polarization Radar Applications, Journal of Atmospheric and Oceanic Technology, 32, 22–47, https://doi.org/10.1175/JTECH-D-14-00097.1, 2015.

Besic, N., Figueras I Ventura, J., Grazioli, J., Gabella, M., Germann, U., and Berne, A.: Hydrometeor classification through statistical clustering of polarimetric radar measurements: a semi-supervised approach, Atmospheric Measurement Techniques, 9, 4425–4445, https://doi.org/10.5194/amt-9-4425-2016, 2016.

Blevis, B.: Losses due to rain on radomes and antenna reflecting surfaces, IEEE Transactions on Antennas and Propagation, 13, 175–176, https://doi.org/10.1109/TAP.1965.1138384, 1965.

Boodoo, S., Hudak, D., Donaldson, N., and Leduc, M.: Application of Dual-Polarization Radar Melting-Layer Detection Algorithm, Journal of Applied Meteorology and Climatology, 49, 1779–1793, https://doi.org/10.1175/2010JAMC2421.1, 2010.

Brandes, E. A., Zhang, G., and Vivekanandan, J.: Experiments in Rainfall Estimation with a Polarimetric Radar in a Subtropical Environment, Journal of Applied Meteorology, 41, 674–685, https://doi.org/10.1175/1520-0450(2002)041<0674:EIREWA>2.0.CO;2, 2002.

Bringi, V., Thurai, M., Nakagawa, K., Huang, G., Kobayashi, T., Adachi, A., Hanado, H., and Sekizawa, S.: Rainfall Estimation from C-Band Polarimetric Radar in Okinawa, Japan: Comparisons with 2D-Video Disdrometer and 400 MHz Wind Profiler, Journal of the Meteorological Society of Japan. Ser. II, 84, 705–724, https://doi.org/10.2151/jmsj.84.705, 2006.

Bringi, V. N. and Chandrasekar, V.: Polarimetric Doppler weather radar: principles and applications, Cambridge University Press, Cambridge, oCLC: 934243039, 2001.

Bringi, V. N., Rico-Ramirez, M. A., and Thurai, M.: Rainfall Estimation with an Operational Polarimetric C-Band Radar in the United Kingdom: Comparison with a Gauge Network and Error Analysis, Journal of Hydrometeorology, 12, 935–954, https://doi.org/10.1175/JHM-D-10-05013.1, 2011.

Carey, L. D., Rutledge, S. A., Ahijevych, D. A., and Keenan, T. D.: Correcting Propagation Effects in C-Band Polarimetric Radar Observations of Tropical Convection Using Differential Propagation Phase, Journal of Applied Meteorology, 39, 1405–1433, https://doi.org/10.1175/1520-0450(2000)039<1405:CPEICB>2.0.CO;2, 2000.

605   Chandrasekar, V., Bringi, V. N., Balakrishnan, N., and Zrnić, D. S.: Error Structure of Multiparameter Radar and Surface Measurements of Rainfall. Part III: Specific Differential Phase, Journal of Atmospheric and Oceanic Technology, 7, 621–629, https://doi.org/10.1175/1520-0426(1990)007<0621:ESOMRA>2.0.CO;2, 1990.

Chandrasekar, V., Keränen, R., Lim, S., and Moisseev, D.: Recent advances in classification of observations from dual polarization weather radars, Atmospheric Research, 119, 97–111, https://doi.org/10.1016/j.atmosres.2011.08.014, 2013.

610   Chen, H. and Chandrasekar, V.: The quantitative precipitation estimation system for Dallas–Fort Worth (DFW) urban remote sensing network, Journal of Hydrology, 531, 259–271, https://doi.org/10.1016/j.jhydrol.2015.05.040, 2015.

Chen, H., Chandrasekar, V., and Bechini, R.: An Improved Dual-Polarization Radar Rainfall Algorithm (DROPS2.0): Application in NASA IFloodS Field Campaign, Journal of Hydrometeorology, 18, 917–937, https://doi.org/10.1175/JHM-D-16-0124.1, 2017.

Cifelli, R., Chandrasekar, V., Lim, S., Kennedy, P. C., Wang, Y., and Rutledge, S. A.: A New Dual-Polarization Radar Rain-
615   fall Algorithm: Application in Colorado Precipitation Events, Journal of Atmospheric and Oceanic Technology, 28, 352–364, https://doi.org/10.1175/2010JTECHA1488.1, 2011.

Cremonini, R., Voormansik, T., Post, P., and Moisseev, D.: Estimation of extreme precipitation events in Estonia and Italy using dual-polarization weather radar quantitative precipitation estimations, Atmospheric Measurement Techniques, 16, 2943–2956, https://doi.org/10.5194/amt-16-2943-2023, 2023.

620   Dolan, B. and Rutledge, S. A.: A Theory-Based Hydrometeor Identification Algorithm for X-Band Polarimetric Radars, Journal of Atmospheric and Oceanic Technology, 26, 2071–2088, https://doi.org/10.1175/2009JTECHA1208.1, 2009.

Dolan, B., Rutledge, S. A., Lim, S., Chandrasekar, V., and Thurai, M.: A Robust C-Band Hydrometeor Identification Algorithm and Application to a Long-Term Polarimetric Radar Dataset, Journal of Applied Meteorology and Climatology, 52, 2162–2186, https://doi.org/10.1175/JAMC-D-12-0275.1, 2013.

625   Du, M., Gao, J., Zhang, G., Wang, Y., Heiselman, P. L., and Cui, C.: Assimilation of Polarimetric Radar Data in Simulation of a Supercell Storm with a Variational Approach and the WRF Model, Remote Sensing, 13, 3060, https://doi.org/10.3390/rs13163060, 2021.

Figueras I Ventura, J. and Tabary, P.: The New French Operational Polarimetric Radar Rainfall Rate Product, Journal of Applied Meteorology and Climatology, 52, 1817–1835, https://doi.org/10.1175/JAMC-D-12-0179.1, 2013.

Giangrande, S. E. and Ryzhkov, A. V.: Estimation of Rainfall Based on the Results of Polarimetric Echo Classification, Journal of Applied
630   Meteorology and Climatology, 47, 2445–2462, https://doi.org/10.1175/2008JAMC1753.1, 2008.

Giangrande, S. E., Krause, J. M., and Ryzhkov, A. V.: Automatic Designation of the Melting Layer with a Polarimetric Prototype of the WSR-88D Radar, Journal of Applied Meteorology and Climatology, 47, 1354–1364, https://doi.org/10.1175/2007JAMC1634.1, 2008.

Giangrande, S. E., McGraw, R., and Lei, L.: An Application of Linear Programming to Polarimetric Radar Differential Phase Processing, Journal of Atmospheric and Oceanic Technology, 30, 1716–1729, https://doi.org/10.1175/JTECH-D-12-00147.1, 2013.

635   Goddard, J., Tan, J., and Thurai, M.: Technique for calibration of meteorological radars using differential phase, Electronics Letters, 30, 166–167, https://doi.org/10.1049/el:19940119, 1994.

Gorgucci, E., Scarchilli, G., and Chandrasekar, V.: Calibration of radars using polarimetric techniques, IEEE Transactions on Geoscience and Remote Sensing, 30, 853–858, https://doi.org/10.1109/36.175319, 1992.

Gourley, J. J., Illingworth, A. J., and Tabary, P.: Absolute Calibration of Radar Reflectivity Using Redundancy of the Polariza-
640   tion Observations and Implied Constraints on Drop Shapes, Journal of Atmospheric and Oceanic Technology, 26, 689–703, https://doi.org/10.1175/2008JTECHA1152.1, 2009.

Grazioli, J., Tuia, D., and Berne, A.: Hydrometeor classification from polarimetric radar measurements: a clustering approach, Atmospheric Measurement Techniques, 8, 149–170, https://doi.org/10.5194/amt-8-149-2015, 2015.

Heistermann, M., Jacobi, S., and Pfaff, T.: Technical Note: An open source library for processing weather radar data (<i>wradlib</i>), Hydrology and Earth System Sciences, 17, 863–871, https://doi.org/10.5194/hess-17-863-2013, 2013.

Helmus, J. J. and Collis, S. M.: The Python ARM Radar Toolkit (Py-ART), a Library for Working with Weather Radar Data in the Python Programming Language, Journal of Open Research Software, 4, 25, https://doi.org/10.5334/jors.119, 2016.

Hickman, B.: Precipitation estimation in urban areas by employing a dense-network of weather radars, M.Sci Thesis, University of Helsinki, Helsinki, http://urn.fi/URN:NBN:fi-fe2017112251840, 2015.

Holleman, I., Huuskonen, A., and Taylor, B.: Solar Monitoring of the NEXRAD WSR-88D Network Using Operational Scan Data, Journal of Atmospheric and Oceanic Technology, 39, 125–139, https://doi.org/10.1175/JTECH-D-20-0204.1, 2022.

Huang, H., Zhang, G., Zhao, K., and Giangrande, S. E.: A Hybrid Method to Estimate Specific Differential Phase and Rainfall With Linear Programming and Physics Constraints, IEEE Transactions on Geoscience and Remote Sensing, 55, 96–111, https://doi.org/10.1109/TGRS.2016.2596295, 2017.

Hubbert, J. and Bringi, V. N.: An Iterative Filtering Technique for the Analysis of Copolar Differential Phase and Dual-Frequency Radar Measurements, Journal of Atmospheric and Oceanic Technology, 12, 643–648, https://doi.org/10.1175/1520-0426(1995)012<0643:AIFTFT>2.0.CO;2, 1995.

Hubbert, J., Chandrasekar, V., Bringi, V. N., and Meischner, P.: Processing and Interpretation of Coherent Dual-Polarized Radar Measurements, Journal of Atmospheric and Oceanic Technology, 10, 155–164, https://doi.org/10.1175/1520-0426(1993)010<0155:PAIOCD>2.0.CO;2, 1993.

Huuskonen, A. and Holleman, I.: Determining Weather Radar Antenna Pointing Using Signals Detected from the Sun at Low Antenna Elevations, Journal of Atmospheric and Oceanic Technology, 24, 476–483, https://doi.org/10.1175/JTECH1978.1, 2007.

Höller, H., Hagen, M., Meischner, P. F., Bringi, V. N., and Hubbert, J.: Life Cycle and Precipitation Formation in a Hybrid-Type Hailstorm Revealed by Polarimetric and Doppler Radar Measurements, Journal of the Atmospheric Sciences, 51, 2500–2522, https://doi.org/10.1175/1520-0469(1994)051<2500:LCAPFI>2.0.CO;2, 1994.

I. Mishchenko, M., Travis, L. D., and Macke, A.: T-Matrix Method and Its Applications, in: Light Scattering by Nonspherical Particles, pp. 147–172, Elsevier, https://doi.org/10.1016/B978-012498660-2/50033-1, 2000.

Illingworth, A.: Improved Precipitation Rates and Data Quality by Using Polarimetric Measurements, in: Weather Radar, edited by Guzzi, R., Imboden, D., Lanzerotti, L. J., Platt, U., and Meischner, P., pp. 130–166, Springer Berlin Heidelberg, Berlin, Heidelberg, https://doi.org/10.1007/978-3-662-05202-0_5, 2004.

Illingworth, A. J. and Blackman, T. M.: The Need to Represent Raindrop Size Spectra as Normalized Gamma Distributions for the Interpretation of Polarization Radar Observations, Journal of Applied Meteorology, 41, 286–297, https://doi.org/10.1175/1520-0450(2002)041<0286:TNTRRS>2.0.CO;2, 2002.

Keenan, T. D.: Hydrometeor classification with a C-Band polarimetric radar, Australian Meteorological Magazine, 52, 23–31, 2003.

Kennedy, P. C. and Rutledge, S. A.: S-Band Dual-Polarization Radar Observations of Winter Storms, Journal of Applied Meteorology and Climatology, 50, 844–858, https://doi.org/10.1175/2010JAMC2558.1, 2011.

Kumjian, M.: Principles and applications of dual-polarization weather radar. Part III: Artifacts, Journal of Operational Meteorology, 1, 265–274, https://doi.org/10.15191/nwajom.2013.0121, 2013.

Kumjian, M. R.: Weather Radars, in: Remote Sensing of Clouds and Precipitation, edited by Andronache, C., pp. 15–63, Springer International Publishing, Cham, https://doi.org/10.1007/978-3-319-72583-3_2, series Title: Springer Remote Sensing/Photogrammetry, 2018.

Kumjian, M. R. and Lombardo, K. A.: Insights into the Evolving Microphysical and Kinematic Structure of Northeastern U.S. Winter Storms from Dual-Polarization Doppler Radar, Monthly Weather Review, 145, 1033–1061, https://doi.org/10.1175/MWR-D-15-0451.1, 2017.

Kumjian, M. R., Lebo, Z. J., and Ward, A. M.: Storms Producing Large Accumulations of Small Hail, Journal of Applied Meteorology and Climatology, 58, 341–364, https://doi.org/10.1175/JAMC-D-18-0073.1, 2019.

Kurri, M. and Huuskonen, A.: Measurements of the Transmission Loss of a Radome at Different Rain Intensities, Journal of Atmospheric and Oceanic Technology, 25, 1590–1599, https://doi.org/10.1175/2008JTECHA1056.1, 2008.

Leinonen, J.: High-level interface to T-matrix scattering calculations: architecture, capabilities and limitations, Optics Express, 22, 1655, https://doi.org/10.1364/OE.22.001655, 2014.

Leinonen, J., Moisseev, D., Leskinen, M., and Petersen, W. A.: A Climatology of Disdrometer Measurements of Rainfall in Finland over Five Years with Implications for Global Radar Observations, Journal of Applied Meteorology and Climatology, 51, 392–404, https://doi.org/10.1175/JAMC-D-11-056.1, 2012.

Li, H., Moisseev, D., Luo, Y., Liu, L., Ruan, Z., Cui, L., and Bao, X.: Assessing specific differential phase (K_{DP})-based quantitative precipitation estimation for the record- breaking rainfall over Zhengzhou city on 20 July 2021, Hydrology and Earth System Sciences, 27, 1033–1046, https://doi.org/10.5194/hess-27-1033-2023, 2023.

Lim, S., Chandrasekar, V., and Bringi, V.: Hydrometeor classification system using dual-polarization radar measurements: model improvements and in situ verification, IEEE Transactions on Geoscience and Remote Sensing, 43, 792–801, https://doi.org/10.1109/TGRS.2004.843077, 2005.

Liu, H. and Chandrasekar, V.: Classification of Hydrometeors Based on Polarimetric Radar Measurements: Development of Fuzzy Logic and Neuro-Fuzzy Systems, and In Situ Verification, Journal of Atmospheric and Oceanic Technology, 17, 140–164, https://doi.org/10.1175/1520-0426(2000)017<0140:COHBOP>2.0.CO;2, 2000.

Maesaka, T., Iwanami, K., and Maki, M.: Non-negative KDP estimation by monotone increasing ΦDP assumption below melting layer, Touluse, http://www.meteo.fr/cic/meetings/2012/ERAD/extended_abs/QPE_233_ext_abs.pdf, 2012.

Marzano, F. S., Scaranari, D., and Vulpiani, G.: Supervised Fuzzy-Logic Classification of Hydrometeors Using C-Band Weather Radars, IEEE Transactions on Geoscience and Remote Sensing, 45, 3784–3799, https://doi.org/10.1109/TGRS.2007.903399, 2007.

Matrosov, S. Y., Cifelli, R., Kennedy, P. C., Nesbitt, S. W., Rutledge, S. A., Bringi, V. N., and Martner, B. E.: A Comparative Study of Rainfall Retrievals Based on Specific Differential Phase Shifts at X- and S-Band Radar Frequencies, Journal of Atmospheric and Oceanic Technology, 23, 952–963, https://doi.org/10.1175/JTECH1887.1, 2006.

May, P. T., Keenan, T. D., Zrnić, D. S., Carey, L. D., and Rutledge, S. A.: Polarimetric Radar Measurements of Tropical Rain at a 5-cm Wavelength, Journal of Applied Meteorology, 38, 750–765, https://doi.org/10.1175/1520-0450(1999)038<0750:PRMOTR>2.0.CO;2, 1999.

Moisseev, D. N.: FMI Parsivel23, https://hdl.handle.net/21.12132/3.69dddc0004b64b32, 2024.

Moisseev, D. N., Lautaportti, S., Tyynela, J., and Lim, S.: Dual-polarization radar signatures in snowstorms: Role of snowflake aggregation, Journal of Geophysical Research: Atmospheres, 120, 12 644–12 655, https://doi.org/10.1002/2015JD023884, 2015.

Otto, T. and Russchenberg, H. W. J.: Estimation of Specific Differential Phase and Differential Backscatter Phase From Polarimetric Weather Radar Measurements of Rain, IEEE Geoscience and Remote Sensing Letters, 8, 988–992, https://doi.org/10.1109/LGRS.2011.2145354, 2011.

Oue, M., Kumjian, M. R., Lu, Y., Jiang, Z., Clothiaux, E. E., Verlinde, J., and Aydin, K.: X-Band Polarimetric and Ka-Band Doppler Spectral Radar Observations of a Graupel-Producing Arctic Mixed-Phase Cloud, Journal of Applied Meteorology and Climatology, 54, 1335–1351, https://doi.org/10.1175/JAMC-D-14-0315.1, 2015.

720 Park, H. S., Ryzhkov, A. V., Zrnić, D. S., and Kim, K.-E.: The Hydrometeor Classification Algorithm for the Polarimetric WSR-88D: Description and Application to an MCS, Weather and Forecasting, 24, 730–748, https://doi.org/10.1175/2008WAF2222205.1, 2009.

Ramdas, A., Garcia, N., and Cuturi, M.: On Wasserstein Two Sample Testing and Related Families of Nonparametric Tests, https://doi.org/10.48550/ARXIV.1509.02237, version Number: 2, 2015.

Reimel, K. J. and Kumjian, M.: Evaluation of KDP Estimation Algorithm Performance in Rain Using a Known-Truth Framework, Journal

725 of Atmospheric and Oceanic Technology, 38, 587–605, https://doi.org/10.1175/JTECH-D-20-0060.1, 2021.

Reinoso-Rondinel, R., Unal, C., and Russchenberg, H.: Adaptive and High-Resolution Estimation of Specific Differential Phase for Polarimetric X-Band Weather Radars, Journal of Atmospheric and Oceanic Technology, 35, 555–573, https://doi.org/10.1175/JTECH-D-17-0105.1, 2018.

Ribaud, J.-F., Machado, L. A. T., and Biscaro, T.: X-band dual-polarization radar-based hydrometeor classification for Brazilian tropical

730 precipitation systems, Atmospheric Measurement Techniques, 12, 811–837, https://doi.org/10.5194/amt-12-811-2019, 2019.

Ryzhkov, A. and Zrnic, D.: Beamwidth Effects on the Differential Phase Measurements of Rain, Journal of Atmospheric and Oceanic Technology, 15, 624–634, https://doi.org/10.1175/1520-0426(1998)015<0624:BEOTDP>2.0.CO;2, 1998.

Ryzhkov, A. and Zrnić, D.: Assessment of Rainfall Measurement That Uses Specific Differential Phase, Journal of Applied Meteorology, 35, 2080–2090, https://doi.org/10.1175/1520-0450(1996)035<2080:AORMTU>2.0.CO;2, 1996.

735 Ryzhkov, A. V. and Zrnic, D. S.: Radar Polarimetry for Weather Observations, Springer Atmospheric Sciences, Springer International Publishing : Imprint: Springer, Cham, 1st ed. 2019 edn., https://doi.org/10.1007/978-3-030-05093-1, 2019.

Ryzhkov, A. V. and Zrnić, D. S.: Comparison of Dual-Polarization Radar Estimators of Rain, Journal of Atmospheric and Oceanic Technology, 12, 249–256, https://doi.org/10.1175/1520-0426(1995)012<0249:CODPRE>2.0.CO;2, 1995.

Ryzhkov, A. V., Giangrande, S. E., Melnikov, V. M., and Schuur, T. J.: Calibration Issues of Dual-Polarization Radar Measurements, Journal

740 of Atmospheric and Oceanic Technology, 22, 1138–1155, https://doi.org/10.1175/JTECH1772.1, 2005a.

Ryzhkov, A. V., Giangrande, S. E., and Schuur, T. J.: Rainfall Estimation with a Polarimetric Prototype of WSR-88D, Journal of Applied Meteorology, 44, 502–515, https://doi.org/10.1175/JAM2213.1, 2005b.

Ryzhkov, A. V., Schuur, T. J., Burgess, D. W., Heinselman, P. L., Giangrande, S. E., and Zrnic, D. S.: The Joint Polarization Experiment: Polarimetric Rainfall Measurements and Hydrometeor Classification, Bulletin of the American Meteorological Society, 86, 809–824,

745 https://doi.org/10.1175/BAMS-86-6-809, 2005c.

Sachidananda, M. and Zrnić, D. S.: Rain Rate Estimates from Differential Polarization Measurements, Journal of Atmospheric and Oceanic Technology, 4, 588–598, https://doi.org/10.1175/1520-0426(1987)004<0588:RREFDP>2.0.CO;2, 1987.

Scarchilli, G., Goroucci, E., Chandrasekar, V., and Seliga, T. A.: Rainfall Estimation Using Polarimetric Techniques at C-Band Frequencies, Journal of Applied Meteorology, 32, 1150–1160, https://doi.org/10.1175/1520-0450(1993)032<1150:REUPTA>2.0.CO;2, 1993.

750 Scarchilli, G., Gorgucci, V., Chandrasekar, V., and Dobaie, A.: Self-consistency of polarization diversity measurement of rainfall, IEEE Transactions on Geoscience and Remote Sensing, 34, 22–26, https://doi.org/10.1109/36.481887, 1996.

Schneebeli, M. and Berne, A.: An Extended Kalman Filter Framework for Polarimetric X-Band Weather Radar Data Processing, Journal of Atmospheric and Oceanic Technology, 29, 711–730, https://doi.org/10.1175/JTECH-D-10-05053.1, 2012.

Schneebeli, M., Dawes, N., Lehning, M., and Berne, A.: High-Resolution Vertical Profiles of X-Band Polarimetric Radar Observables during Snowfall in the Swiss Alps, Journal of Applied Meteorology and Climatology, 52, 378–394, https://doi.org/10.1175/JAMC-D-12-015.1, 2013.

Schneebeli, M., Grazioli, J., and Berne, A.: Improved Estimation of the Specific Differential Phase Shift Using a Compilation of Kalman Filter Ensembles, IEEE Transactions on Geoscience and Remote Sensing, 52, 5137–5149, https://doi.org/10.1109/TGRS.2013.2287017, 2014.

Snyder, J. C., Bluestein, H. B., Zhang, G., and Frasier, S. J.: Attenuation Correction and Hydrometeor Classification of High-Resolution, X-band, Dual-Polarized Mobile Radar Measurements in Severe Convective Storms, Journal of Atmospheric and Oceanic Technology, 27, 1979–2001, https://doi.org/10.1175/2010JTECHA1356.1, 2010.

Tapping, K. F.: The 10.7 cm solar radio flux ($F_{10.7}$), Space Weather, 11, 394–406, https://doi.org/10.1002/swe.20064, 2013.

Tessendorf, S. A., Miller, L. J., Wiens, K. C., and Rutledge, S. A.: The 29 June 2000 Supercell Observed during STEPS. Part I: Kinematics and Microphysics, Journal of the Atmospheric Sciences, 62, 4127–4150, https://doi.org/10.1175/JAS3585.1, 2005.

Thomas, G., Mahfouf, J.-F., and Montmerle, T.: Toward a variational assimilation of polarimetric radar observations in a convective-scale numerical weather prediction (NWP) model, Atmospheric Measurement Techniques, 13, 2279–2298, https://doi.org/10.5194/amt-13-2279-2020, 2020.

Thompson, E. J., Rutledge, S. A., Dolan, B., Chandrasekar, V., and Cheong, B. L.: A Dual-Polarization Radar Hydrometeor Classification Algorithm for Winter Precipitation, Journal of Atmospheric and Oceanic Technology, 31, 1457–1481, https://doi.org/10.1175/JTECH-D-13-00119.1, 2014.

Thompson, E. J., Rutledge, S. A., Dolan, B., Thurai, M., and Chandrasekar, V.: Dual-Polarization Radar Rainfall Estimation over Tropical Oceans, Journal of Applied Meteorology and Climatology, 57, 755–775, https://doi.org/10.1175/JAMC-D-17-0160.1, 2018.

Thurai, M. and Bringi, V. N.: Drop Axis Ratios from a 2D Video Disdrometer, Journal of Atmospheric and Oceanic Technology, 22, 966–978, https://doi.org/10.1175/JTECH1767.1, 2005.

Thurai, M., Huang, G. J., Bringi, V. N., Randeu, W. L., and Schönhuber, M.: Drop Shapes, Model Comparisons, and Calculations of Polarimetric Radar Parameters in Rain, Journal of Atmospheric and Oceanic Technology, 24, 1019–1032, https://doi.org/10.1175/JTECH2051.1, 2007.

Tiira, J. and Moisseev, D.: Unsupervised classification of vertical profiles of dual polarization radar variables, Atmospheric Measurement Techniques, 13, 1227–1241, https://doi.org/10.5194/amt-13-1227-2020, 2020.

Vaisala: IRIS (version 8.13), www.vaisala.com, 2017.

Virtanen, P., Gommers, R., Oliphant, T. E., Haberland, M., Reddy, T., Cournapeau, D., Burovski, E., Peterson, P., Weckesser, W., Bright, J., Van Der Walt, S. J., Brett, M., Wilson, J., Millman, K. J., Mayorov, N., Nelson, A. R. J., Jones, E., Kern, R., Larson, E., Carey, C. J., Polat, , Feng, Y., Moore, E. W., VanderPlas, J., Laxalde, D., Perktold, J., Cimrman, R., Henriksen, I., Quintero, E. A., Harris, C. R., Archibald, A. M., Ribeiro, A. H., Pedregosa, F., Van Mulbregt, P., SciPy 1.0 Contributors, Vijaykumar, A., Bardelli, A. P., Rothberg, A., Hilboll, A., Kloeckner, A., Scopatz, A., Lee, A., Rokem, A., Woods, C. N., Fulton, C., Masson, C., Häggström, C., Fitzgerald, C., Nicholson, D. A., Hagen, D. R., Pasechnik, D. V., Olivetti, E., Martin, E., Wieser, E., Silva, F., Lenders, F., Wilhelm, F., Young, G., Price, G. A., Ingold, G.-L., Allen, G. E., Lee, G. R., Audren, H., Probst, I., Dietrich, J. P., Silterra, J., Webber, J. T., Slavič, J., Nothman, J., Buchner, J., Kulick, J., Schönberger, J. L., De Miranda Cardoso, J. V., Reimer, J., Harrington, J., Rodríguez, J. L. C., Nunez-Iglesias, J., Kuczynski, J., Tritz, K., Thoma, M., Newville, M., Kümmerer, M., Bolingbroke, M., Tartre, M., Pak, M., Smith, N. J., Nowaczyk, N., Shebanov, N., Pavlyk, O., Brodtkorb, P. A., Lee, P., McGibbon, R. T., Feldbauer, R., Lewis, S., Tygier, S., Sievert, S., Vigna, S., Peterson, S., More,

S., Pudlik, T., Oshima, T., Pingel, T. J., Robitaille, T. P., Spura, T., Jones, T. R., Cera, T., Leslie, T., Zito, T., Krauss, T., Upadhyay, U., Halchenko, Y. O., and Vázquez-Baeza, Y.: SciPy 1.0: fundamental algorithms for scientific computing in Python, Nature Methods, 17, 261–272, https://doi.org/10.1038/s41592-019-0686-2, 2020.

Vivekanandan, J., Ellis, S. M., Oye, R., Zrnic, D. S., Ryzhkov, A. V., and Straka, J.: Cloud Microphysics Retrieval Using S-band Dual-Polarization Radar Measurements, Bulletin of the American Meteorological Society, 80, 381–388, https://doi.org/10.1175/1520-0477(1999)080<0381:CMRUSB>2.0.CO;2, 1999.

Vivekanandan, J., Zhang, G., Ellis, S. M., Rajopadhyaya, D., and Avery, S. K.: Radar reflectivity calibration using differential propagation phase measurement: RADAR REFLECTIVITY CALIBRATION, Radio Science, 38, n/a–n/a, https://doi.org/10.1029/2002RS002676, 2003.

Vulpiani, G., Montopoli, M., Passeri, L. D., Gioia, A. G., Giordano, P., and Marzano, F. S.: On the Use of Dual-Polarized C-Band Radar for Operational Rainfall Retrieval in Mountainous Areas, Journal of Applied Meteorology and Climatology, 51, 405–425, https://doi.org/10.1175/JAMC-D-10-05024.1, 2012.

Wang, Y. and Chandrasekar, V.: Algorithm for Estimation of the Specific Differential Phase, Journal of Atmospheric and Oceanic Technology, 26, 2565–2578, https://doi.org/10.1175/2009JTECHA1358.1, 2009.

Wang, Y., Zhang, J., Ryzhkov, A. V., and Tang, L.: C-Band Polarimetric Radar QPE Based on Specific Differential Propagation Phase for Extreme Typhoon Rainfall, Journal of Atmospheric and Oceanic Technology, 30, 1354–1370, https://doi.org/10.1175/JTECH-D-12-00083.1, 2013.

Waterman, P.: Matrix formulation of electromagnetic scattering, Proceedings of the IEEE, 53, 805–812, https://doi.org/10.1109/PROC.1965.4058, 1965.

Wen, G., Protat, A., May, P. T., Wang, X., and Moran, W.: A Cluster-Based Method for Hydrometeor Classification Using Polarimetric Variables. Part I: Interpretation and Analysis, Journal of Atmospheric and Oceanic Technology, 32, 1320–1340, https://doi.org/10.1175/JTECH-D-13-00178.1, 2015.

Wen, G., Fox, N. I., and Market, P. S.: A Gaussian mixture method for specific differential phase retrieval at X-band frequency, Atmospheric Measurement Techniques, 12, 5613–5637, https://doi.org/10.5194/amt-12-5613-2019, 2019.

Zhang, J., Tang, L., Cocks, S., Zhang, P., Ryzhkov, A., Howard, K., Langston, C., and Kaney, B.: A Dual-Polarization Radar Synthetic QPE for Operations, Journal of Hydrometeorology, 21, 2507–2521, https://doi.org/10.1175/JHM-D-19-0194.1, 2020.

Zrnić, D. S. and Ryzhkov, A.: Advantages of Rain Measurements Using Specific Differential Phase, Journal of Atmospheric and Oceanic Technology, 13, 454–464, https://doi.org/10.1175/1520-0426(1996)013<0454:AORMUS>2.0.CO;2, 1996.

Zrnić, D. S., Ryzhkov, A., Straka, J., Liu, Y., and Vivekanandan, J.: Testing a Procedure for Automatic Classification of Hydrometeor Types, Journal of Atmospheric and Oceanic Technology, 18, 892–913, https://doi.org/10.1175/1520-0426(2001)018<0892:TAPFAC>2.0.CO;2, 2001.